PARALLEL ACQUISITION IN MULTIPHOTON MICROSCOPY: TEMPORAL FOCUSING AND FREQUENCY MULTIPLEXING

A Dissertation

Presented to the Faculty of the Graduate School

of Cornell University

in Partial Fulfillment of the Requirements for the Degree of

Doctor of Philosophy

by

Adam Arthur Straub

January 2015

PARALLEL ACQUISITION IN MULTIPHOTON MICROSCOPY: TEMPORAL FOCUSING AND FREQUENCY MULTIPLEXING

Adam Arthur Straub

Cornell University 2015

Multiphoton microscopy is a powerful platform for both biological study and medical imaging. Techniques developed on this platform have achieved unparalleled resolution and chemical specificity, imaging at depths unreachable by traditional forms of optical microscopy. This thesis details several techniques meant to improve multiphoton depth penetration, imaging speed, and medical applicability.

One such technique uses a modified form of simultaneous spatial and temporal focusing (SSTF) to achieve enhanced axial confinement. In SSTF a diffraction grating is imaged onto the sample, and the separation and recombination of the excitation spectral components form a temporal focus. By blocking the central portion of the excitation spectrum, an effective two-color two-photon imaging system is formed. By detecting only the resulting sum frequency generation signal the axial confinement becomes significantly tighter than that achieved by conventional two-photon microscopy.

The temporal focus of SSTF may be axially scanned by modulating the group delay dispersion (GDD) of the excitation pulse. In a proof-of-concept experiment, a piezo-bimorph mirror is used to rapidly modulate GDD in a temporal focusing setup. Axial scans over 60 μm of mouse skin are performed at speeds up to 200Hz. This is done through an optical fiber and with

no moving parts or electrical components at the distal end, paving the way for the development of a minimally invasive, axial scanning endoscope.

Another technique uses frequency multiplexing to perform parallel acquisition of image data using a single-element detector. Five hundred pixels in a line are individually intensity modulated at different radio frequencies. A Fourier transform of the signal unscrambles the image data after detection. In scattering regimes where conventional parallel acquisition (i.e. charge coupled device array, or CCD) methods are impossible, this multifocal multiphoton modulation microscopy (M4) technique allows for higher signal-to-noise ratios and faster imaging. Fluorescent/phosphorescent lifetime can be calculated from the phase component of the Fourier transform in the M4 technique. In combination with the inherent speed advantages of M4, this is used to take full-frame phosphorescent lifetime images of oxygen-sensing dye *in* vivo in mouse brain vasculature at record speed.

BIOGRAPHICAL SKETCH

Adam Straub was born in June of 1984, and grew up in South Berwick, Maine, a small town of fewer than seven thousand residents. His parents, William and Gretchen Straub, raised him along with his brother, Brian. He attended the local public school system, shared with the neighboring town of Eliot, where he graduated in 2002.

He attended Brown University, in Rhode Island, where he was encouraged to choose among his first-semester courses at least one course, "just for fun." Adam chose a course in Newtonian mechanics, not realizing it was meant for students with a considerably stronger background in calculus and physics than he had received in high school. He enjoyed the challenge so much he decided to major in physics, and graduated magna cum laude in 2006.

Deciding not to go to graduate school immediately, Adam first travelled to Harbin, China. He lived there for six months studying Mandarin and the Chinese board game of Go. He resolved not to speak a word of English while he was there, forcing him to be mostly silent for several weeks. When he returned home in December, he was conversationally fluent in Mandarin and a decent Go player.

In January of 2007 he began work as a product engineer at Xemed, LLC in Durham, New Hampshire, a small startup company developing gas polarization systems. This was a great experience for Adam, learning basic machining, computer aided design, and the nuts and bolts of experimentation and engineering.

That fall he began his graduate education at Cornell University in Ithaca, New York. He began working with Chris Xu in 2008, studying multiphoton microscopy.

ACKNOWLEDGMENTS

My time at Cornell University has been exciting, challenging, at times overwhelming and at others highly fulfilling. Several important people have been instrumental to me in this time, serving as mentors, coworkers, and friends.

When I first joined Chris Xu's group, senior graduate student Michael Durst took me under his wing. I had no formal education in optics, and Mike taught me everything I needed to know to be a productive researcher. From table-top techniques to quickly align a laser beam to lengthy derivations for propagating a wave front through space, Mike encouraged me to take the time to completely understand everything I encountered before moving on. Furthermore, Mike taught me how to enjoy life as a graduate student - how to balance working and socializing, and the importance of both.

Scott Howard joined the group as a post doc in 2010, and I was fortunate to work closely with him. Scott has an insatiable and contagious curiosity about the workings of any system he encounters. His unique intuition for physics was great asset, and he encouraged me to consider problems in new ways. At the time of writing, Scott is busy spreading his enthusiasm to students and researchers at Notre Dame as a new faculty member.

I want to thank all the members of the Xu group for maintaining a friendly, positive, and inherently curious atmosphere about the lab. Particularly memorable are late-night discussions with Demirhan Kobat about popular technology, my amazement with Ji Cheng's math acumen as he sets me straight on a derivation, David Rivera's rock-solid friendship and work ethic, and Kriti Charan's willingness to thoroughly explore spontaneous physics questions.

Most importantly I want to thank my advisor Chris Xu. His intelligence, character, and ability to quickly reduce any problem to its most basic components are astounding. Group meeting after group meeting, Chris Xu teaches how to effectively understand and solve problems. He excels at identifying the single key component to any issue, and finding a way to work it to advantage. In private, Chris is a caring, honest, and straight-forward man. His intelligence and cooperative nature leads to highly productive discussions, and his guidance and encouragement has helped me through many obstacles, both professional and personal. He draws the best out of those around him by giving himself as an example. Thank-you.

TABLE OF CONTENTS

LIST OF ABBREVIATIONS

2D/3D	Two dimensional / Three dimensional
CARS	Coherent anti-stokes Raman spectroscopy
CCD	Charge coupled device
GDD	Group delay dispersion
M4	Multifocal multiphoton modulation microscopy
MPM	Multiphoton microscopy
MRI	Magnetic resonance imaging
NA	Numerical Aperture
OCT	Optical coherence tomography
PALM	Photo-activated localization microscopy
PLIM	Phosphorescence lifetime imaging microscopy
PMT	Photomultiplier tube
RF	Radio frequency
SFG	Sum frequency generation
SHG	Second harmonic generation
SLM	Spatial light modulator
SNR	Signal to noise ratio
SRS	Stimulated Raman spectroscopy
SSTF	Simultaneous spatial and temporal focusing
STED	Stimulated emission depletion microscopy
THG	Third harmonic generation
TPE	Two photon excitation

CHAPTER 1 :

INTRODUCTION

1.1 Imaging tools and multiphoton microscopy

Many tools exist for the purpose of imaging biological tissue. Each tool's efficacy can be judged on the three metrics of resolution, specificity, and imaging depth. Here I briefly describe the place of multiphoton microscopy (MPM) among this suite of tools, and argue that it provides a worth-while base upon which to develop specialized imaging techniques. I assume that the reader understands the basic mechanisms of MPM. A great overview of MPM is available in the Zipfel, Williams, and Webb review article on "Nonlinear magic" [1].

The most traditional tool for biological imaging is visible-spectrum optical microscopy. With proper equipment, it easily achieves sub-micron resolution, and when combined with antigen-specific fluorescent dyes enables a high degree of chemical specificity. Visible-spectrum optical microscopy may be augmented with techniques such as confocal microscopy, which extend the potential imaging depth from surface-only to over 100 microns [2]. Long-wavelength optical coherence tomography (OCT) can further extend this to several millimeters, at the price of chemical specificity [3].

Other tools such as ultrasound, magnetic resonance imaging (MRI), and x-rays have imaging depths on the order of centimeters or meters (entire body). Unfortunately, specificity and contrast agents for these extreme deep-imaging tools are very limited, and typical resolution is on the order of hundreds of microns. Various techniques can improve resolution and specificity, but not approach that of optical microscopy.

Multiphoton microscopy is an extension of traditional microscopy, its primary advantage being the ability to spatially isolate optical excitation in all three dimensions, allowing for detailed three-dimensional imaging [1]. The imaging depth of MPM in typical biological tissue is on the order of one millimeter, covering tens to hundreds of cell layers depending on the sample [4]. Because the excitation wavelength is long but the signal wavelength is short, MPM achieves the best depth penetration optics can provide while maintaining superior resolution.

MPM retains the chemical specificity of traditional visible -spectrum microscopy due to fluorescence. Additionally, the nonlinear nature of MPM provides a unique contrast mechanism in the form of second harmonic generation (SHG) and third harmonic generation (THG). These signals are generated at exactly half or one third of the excitation wavelength, respectively, and more prevalently in specific types of tissue (e.g. SHG is generated strongly in collagen). These harmonic signals are easily isolated because they are at significantly shorter wavelength than the corresponding fluorescent response, providing yet another source of specificity for MPM. Experiments in depth-resolved tissue spectroscopy and imaging have shown that multiphoton fluorescence and harmonic generation microscopy techniques can effectively be used in cancer detection and diagnostics [5, 6, 7].

Regarding the three metrics of resolution, specificity, and imaging depth, multiphoton microscopy performs extremely well. Typical MPM boasts resolution well under 1 μm, access to both fluorescence and harmonic generation as contrast mechanisms, and imaging depth over 1 mm. This makes MPM the ideal imaging technique for both the metrics of resolution and specificity, and outperforms or meets other optical techniques regarding imaging depth. Consequently MPM is a popular platform for the development of novel imaging techniques. Stimulated emission depletion microscopy (STED) and photo-activated localization microscopy

(PALM) can push MPM resolution to less than 10 nm [8, 9]. Coherent anti-stokes Raman spectroscopy (CARS) and stimulated Raman spectroscopy (SRS) allow for unprecedented chemical specificity, all the while maintaining the three-dimensional imaging capability of MPM [10, 11]. In this thesis I detail techniques that can be used to improve the axial confinement and imaging speed of the MPM platform.

1.2 Simultaneous spatial and temporal focusing

Both of the techniques detailed in chapters 2 and 3 are based on simultaneous spatial and temporal focusing (SSTF). This section provides a summary description of SSTF. A more detailed explanation is available in Durst, *et. al.* [12].

A typical microscopy focal volume is formed by converging light across two dimensions of space onto a diffraction limited focus, its size determined by the numerical aperture (NA) of the objective lens and the wavelength of the light. Because MPM relies on the nonlinear response of the sample, the signal is additionally dependent upon the temporal profile of the excitation pulse. Simultaneous spatial and temporal focusing is a multiphoton technique that uses this temporal dependence to replace one or both of the spatial dimensions used in focusing with a temporal dimension.

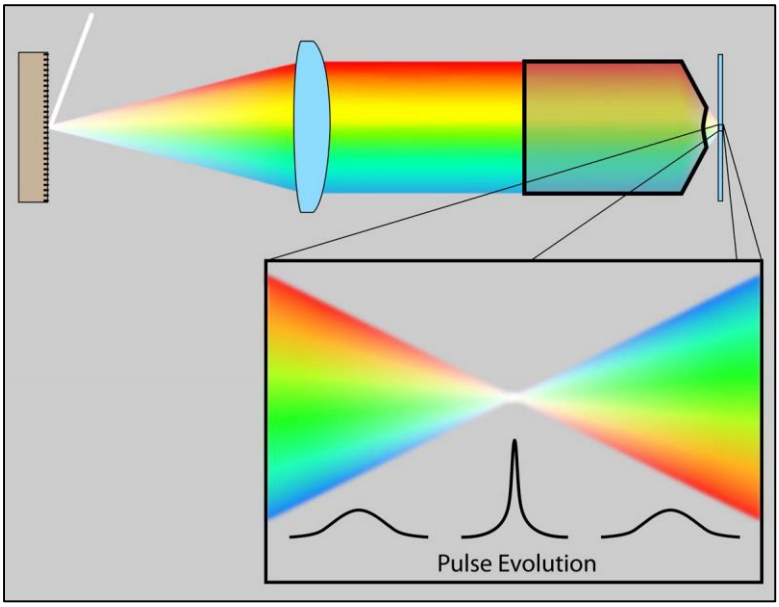

Figure 1.1: Simultaneous spatial and temporal focusing setup and pulse evolution.

In SSTF a diffraction grating is imaged onto the sample, creating a wide-field, temporal focus [13, 14]. As shown in Figure 1.1, the excitation pulse is incident on a diffraction grating, separating the spectral components of the pulse in space. At the back focal plane of the objective lens, each spectral component is separately focused to a small point along a line. Because there is very little spectral overlap, the pulse width at this plane is very long. As they are focused by the objective lens the spectral components recombine, causing the pulse width to vary as a function of axial position. For a transform-limited pulse, the minimum pulse width is recovered at the image plane of the system. Away from the image plane the pulse width broadens quickly. Because two-photon response is inversely proportional to the pulse width, an effective temporal focus is created at the image plane, providing axial confinement of the signal [13, 14].

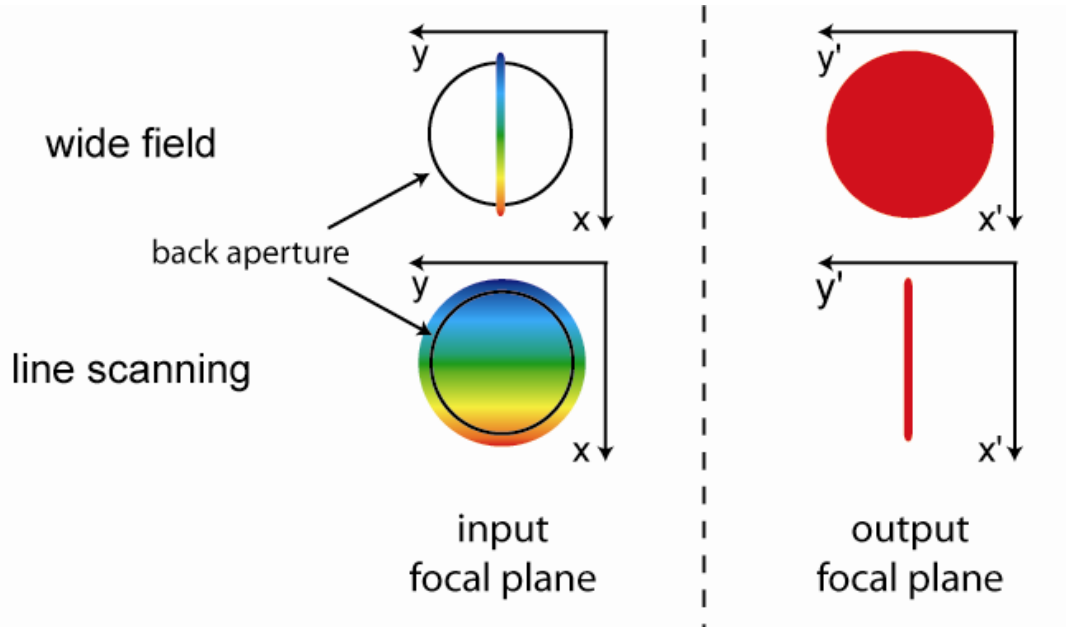

Figure 1.2: Comparison between wide-field and line-scanning SSTF

There are two imaging modalities for SSTF, wide-field and line-scanning, shown in Figure 1.2. Wide-field SSTF illuminates a large viewing area in an axially confined section. Line-scanning SSTF illuminates a single line within the sample, but has tighter axial confinement than the wide-field modality. A complete derivation of the associated focal volumes is available in Durst, *et.al.* [12], the results of which follow.

The standard two-photon excitation (TPE) signal as a function of axial position is given by:

$$TPE_{\text{conventional}}(z) = \frac{C}{1 + \left(\frac{z}{z_R'}\right)^2} \tag{1.1}$$

where C is a constant and z_R is the Rayleigh length given by:

$$z_R' = \frac{2f^2}{kd^2} \tag{1.2}$$

where f is the focal length of the objective lens, k is the wave vector, and $\sqrt{2\ln 2}d$ is the full width half maximum (FWHM) of the beam at the back focal plane of the objective.

The signal from an SSTF focal volume as a function of axial position is similar:

$$TPE_{\mathrm{SSTF}}(z) = \frac{C}{\sqrt{1+\left(\frac{z}{z_R}\right)^2}}\frac{1}{\sqrt{1+\left(\frac{z}{z_M}\right)^2}} \tag{1.3}$$

Here z_R represents the effective Rayleigh length of temporal focusing, coming from the separation of spectral components along the x direction, and is given by:

$$z_R = \frac{2f^2}{k(s^2+\alpha^2\Omega^2)} \tag{1.4}$$

where s and $\alpha\Omega$ are the monochromatic and full-spectrum spot sizes. The second dimension of focusing is characterized by z_M, the Rayleigh length of standard spatial focusing along the y direction, given by:

$$z_M = \frac{2f^2}{kd_y^2} \tag{1.5}$$

where $\sqrt{2\ln 2}d_y$ is the FWHM of the y-dimension of the beam at the back focal plane of the objective.

In the case of line-scanning SSTF, $d_y \approx \alpha\Omega \approx d$, resulting in a similar axial confinement profile to that of traditional two-photon microscopy, that of a Lorentzian. For wide-field microscopy, as shown in Figure 1.2, the back aperture of the objective lens is illuminated by a thin line, so $d_y \approx s$, making z_M so large that the second factor in equation 1.3 may be neglected. Consequently, the axial confinement is not as strong, only a square-root Lorentzian.

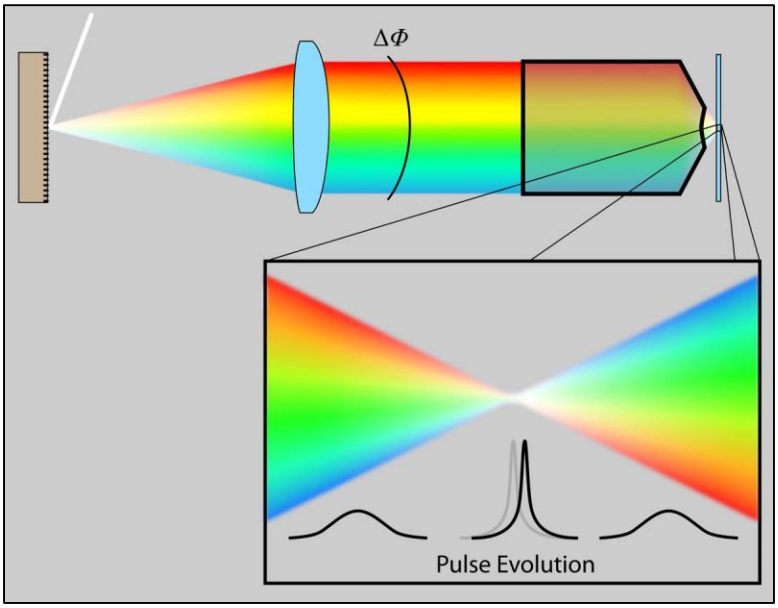

Figure 1.3: Shift in temporal focus of SSTF via group dispersion delay

Because axial confinement in wide-field SSTF derives entirely from the temporal properties of the pulse, the axial focal position may be scanned by altering the pulse temporally rather than spatially. Axial scanning of the temporal focus by changing the group delay dispersion (GDD) of the excitation pulse was experimentally shown and theoretically explained by Durst, *et.al.* [12]. Now including the GDD, the axial two-photon response of a wide-field SSTF system is given approximately by:

$$TPE(z) = \frac{C}{\sqrt{1 + \left(\frac{z + \beta\Omega^2}{z_R}\right)^2}} \tag{1.6}$$

where β is the GDD and $\sqrt{2\ln 2}\,\Omega$ is the FWHM of the pulse spectrum. From this we see that the displacement of the temporal focus is:

$$\Delta z = \beta\Omega^2 \tag{1.7}$$

This capacity to scan the axial position of the focus via GDD opens the possibility for remote axial scanning, as explored in chapter 3.

1.3 Higher speed through frequency multiplexing

Chapter 4 is based on a technique called multifocal multiphoton modulation microscopy (M4). This technique uses frequency multiplexing to perform parallel acquisition of multiple pixels using a single-element detector. An introduction to M4 follows.

Near the surface of a sample, parallel acquisition is easy to perform using detectors such as a charge coupled device (CCD). However, if the focal plane is several scattering lengths deep into the tissue, scattering prevents accurate imaging of signal photons onto the CCD. For this reason a single-element detector such as a photomultiplier tube (PMT) is used to collect all signal photons, and pixel locations are determined by raster scanning the sample with a single excitation point, each pixel serially illuminated in time. While effective at isolating individual pixels, serial acquisition of image data introduces speed limitations that are not shared by parallel acquisition systems.

Under the constraint of a single-element detector, it is possible to achieve parallel acquisition through frequency multiplexing. By tagging each pixel with an individual radio frequency (RF) modulation, all pixels may be simultaneously acquired and then separated via Fourier transform in post-processing.

Consider a set of pixels where each pixel *i* is exposed to the following illumination:

$$I_i(t) = I_0\big(1 + \sin(\omega_i t)\big) \tag{1.8}$$

where I_0 is the intensity of the field and ω_i is the angular frequency of RF modulation. Note that we are leaving out the fast oscillation of the light itself for simplicity. In this case, the signal detected by a single-element detector is given by:

$$S(t) = \sum_i S_i(1 + A\sin(\omega_i t + \theta_i) + B\sin(2\omega_i t + \phi_i)) \qquad (1.9)$$

where S_i indicates the intensity of the *i*th pixel, *A* and *B* are constants, and θ_i and ϕ_i are phase delays. Each pixel contributes three terms to the response, all proportional to its intensity: one constant, one modulating at ω_i, and one modulating at $2\omega_i$ due to the nonlinear nature of two-photon microscopy.

If the ω_i are chosen such that there is no interference between any pixels' modulation frequency or harmonics (i.e. all ω_i within one octave), then the relative intensity of each pixel, S_i, may be extracted from equation 1.8 as the amplitude of a Fourier transform.

One way to construct such a system is to illuminate the sample with a line and modulate each point along that line at a distinct RF modulation frequency. Such modulation can be achieved by scanning the line across a patterned photolithography mask and imaging that mask onto the sample, as shown in Figure 1.4.

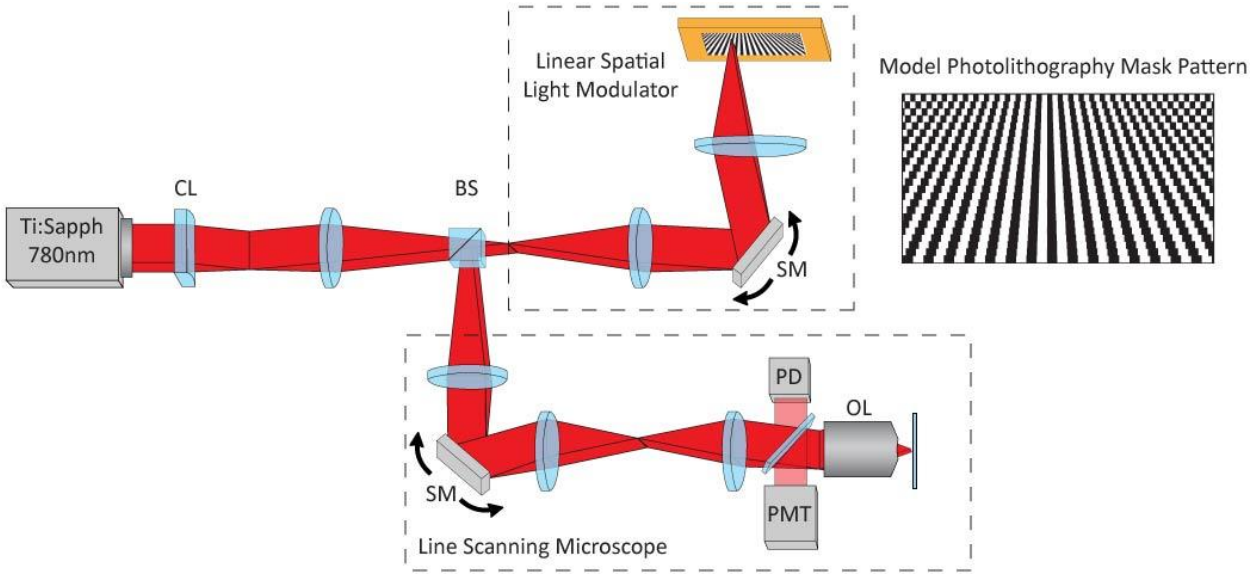

Figure 1.4: Experimental setup for multifocal multiphoton modulation microscopy. CL = cylindrical lens, BS = beam splitter, SM = scan mirror, PD = photodiode, PMT = photomultiplier tube, and OL = objective lens.

Figure 1.5 shows raw data and the post-processed image acquired with such a system of a USAF resolution test chart. In this test, an array of points modulating between 350 and 650 kHz were arranged in a line and incident on the USAF target. The line was then scanned across the target over the course of one second. The raw data was divided into individual time windows 1.5ms long, and each window was Fourier transformed. The result, called a spectrogram, is a reconstruction of the USAF target.

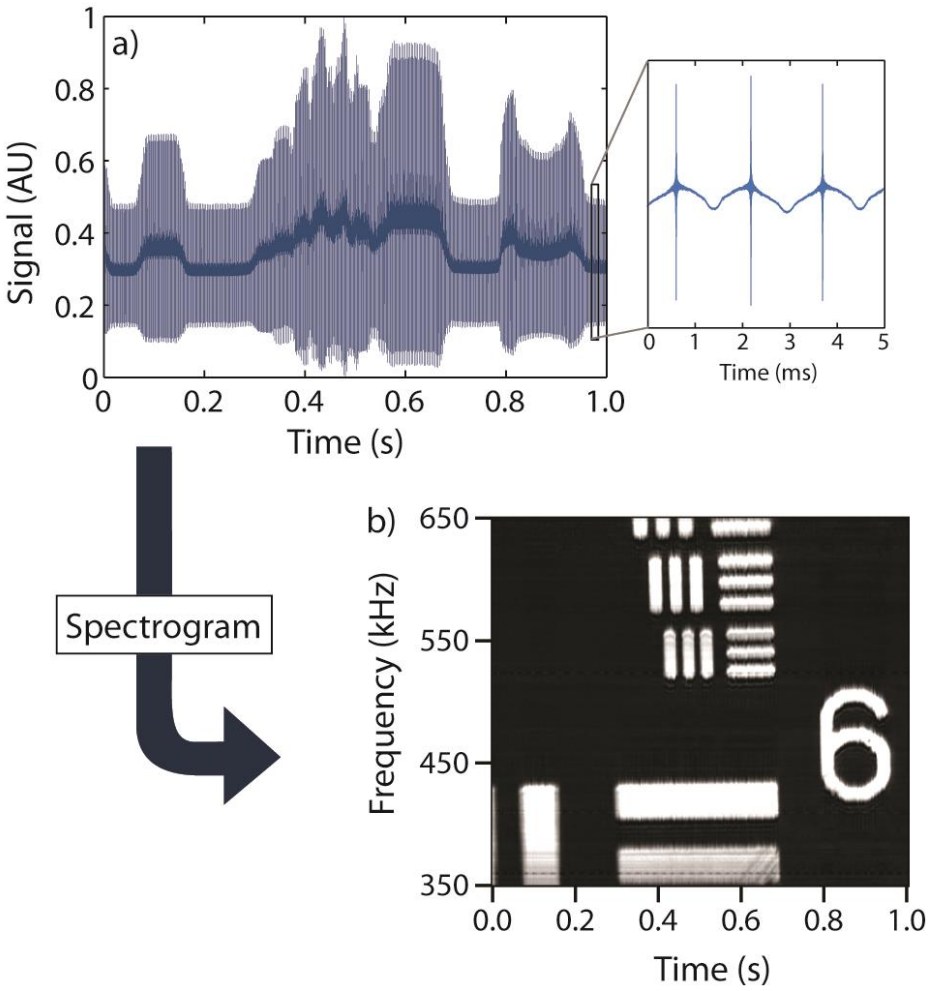

Figure 1.5: Demonstration of the M4 concept by imaging a 1951 USAF Resolution Test Chart and collecting the reflected light signal on a large-area silicon photodiode. The signal at the diode is divided into consecutive time windows corresponding to adjacent image lines with spatial information encoded in the frequency domain. Signal demodulation reconstructs the original image.

This technique introduces new noise terms that are discussed in appendix B. However, it allows for longer integration time over all pixels, ultimately improving signal-to-noise ratio for most imaging targets and a increase in maximum imaging speed.

Modulation microscopy may also be used to measure fluorescent or phosphorescent lifetime. While the amplitude of the Fourier transform is related to pixel intensity, the phase profile of the Fourier transform is linked to lifetime of the pixel by the following equation:

$$\tau_i = \frac{\tan(\theta_i)}{\omega_i} \tag{1.10}$$

As shown in figure 1.6, a non-zero fluorescent lifetime results in a phase delay of the signal given a modulated excitation. This effect is explored more fully in chapter 4.

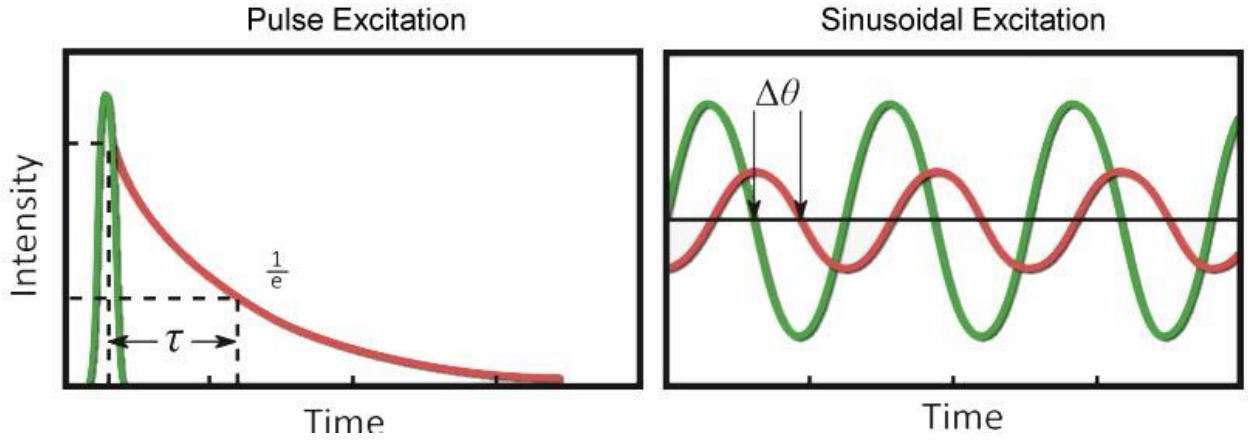

Figure 1.6: Effects of non-zero fluorescent lifetime on fluorophore response given pulse and sinusoidal excitation.

CHAPTER 2 :

ENHANCED AXIAL CONFINEMENT OF SUM FREQUENCY GENERATION IN A TEMPORAL FOCUSING SETUP

2.1 Imaging depth and surface signal

The maximum imaging depth of a multi-photon microscopy system is determined by strength of the multi-photon signal relative to the background. As deeper tissue is imaged, the signal is attenuated exponentially. This is due to scattering and absorption of both excitation and signal photons by the bulk sample, as well as deterioration of the diffraction-limited focus by sample inhomogeneity. The most straight-forward way to recover signal strength is to increase excitation power. However, several scattering-lengths into the sample, the multiphoton signal generated at the surface of the sample becomes comparable to that generated within the focal volume (Figure 2.1). The signal within the focal volume and the 'background' on the surface scale equally with power, so simply increasing excitation power does not solve the problem. This fundamental limiting imaging depth may be extended by choosing an appropriate longer wavelength to minimize scattering and absorption by the sample [4]. While such measures extend the depth penetration of MPM considerably, they do not remove the fundamental issue of surface-signal background noise.

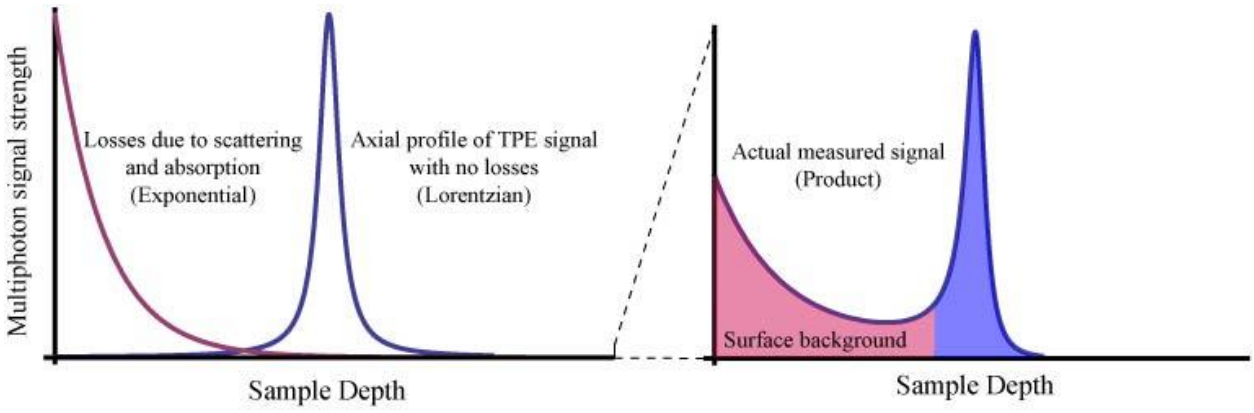

Figure 2.1: Origin of surface-signal background, the product of a Lorentzian axial profile and exponential decay of signal strength.

Several methods have been proposed to enhance the axial confinement of the focal region by suppressing the background due to out-of-focus excitation. Differential aberration imaging measures the background by intentionally eliminating the two-photon excited fluorescence (TPEF) at the focus through added aberrations in the system [15]. The background can then be subtracted from an unaberrated image in order to enhance the signal-to-background ratio. Oron et al. proposed using coherent control to enhance the confinement of simultaneous spatial and temporal focusing (SSTF) [16], in which the frequencies of an ultrashort pulse are spatially separated by a grating and then recombined at the focus [13, 14]. Spectral phase shaping can then selectively turn off the TPEF from the focus in order to measure the out-of-focus background. While both background subtraction techniques demonstrate improved axial confinement, the subtraction operation in fact increases the background-noise contribution due to shot noise. Therefore, background subtraction techniques decrease the signal-to-noise ratio, which is ultimately the limiting factor for imaging performance.

Two-color two-photon (2C2P) microscopy spatially separates the two excitation wavelengths such that no signal corresponding to the sum-frequency generation (SFG) can be

generated outside of the focal region [17, 18, 19]. By filtering the background photons optically, both the background and its associated shot noise are suppressed. The result is a true improvement in signal-to-noise ratio.

2.2 Sum frequency generation with SSTF

Typically, 2C2P microscopy requires two synchronized pulse sources, such as a Ti:sapphire laser pumping an optical parametric oscillator. The pulses at the two wavelengths must be spatially and temporally overlapped in order to observe an SFG effect. This can be prohibitively expensive and complicated. The same effect may be achieved with a single laser source by combining SSTF (see chapter 1 section 2) with 2C2P microscopy. In SSTF, the grating separates the spectral components of the pulse in space, and the two "colors" for a 2C2P setup can be generated by simply blocking the center of the spectrum at the input focal plane of the objective (see Figure 2.2). A theoretical understanding of the SFG process can be found by a coherent summation of the SFG fields due to all the dipole emitters excited within the sample [20, 21, 22]. Owing to the coherent nature of SFG, directionality of emission is highly sample dependent, and in general closed-form analytical solutions cannot be attained. A numerical solution is available by following the rigorous treatment of harmonic imaging with conventional SSTF [23]. Intuitively, the outer spectral components of our spectrally shaped SSTF beam will be spatially overlapped only at the focus, producing an SFG signal at half the center wavelength. By spectrally filtering the collected signal, SHG by the two beams outside the overlapping region is rejected, and only the signal from the common focus is detected, achieving an improved axial confinement.

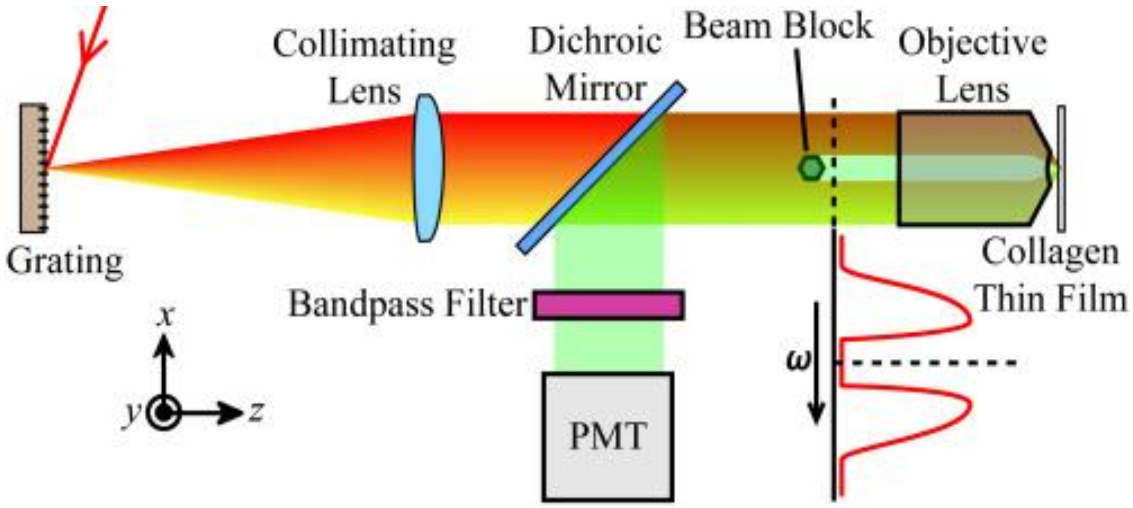

Figure 2.2: Experimental SFG SSTF setup. A grating is imaged onto the sample, with the central portion of the excitation spectrum blocked at the back aperture of the objective lens.

The confinement technique was explored for both imaging modalities of SSTF: wide-field and line-scanning. In the SSTF wide-field case, the beam shape at the input focal plane of the objective is a thin line, where the width in the x direction is the spread of the monochromatic components due to the grating, and the height in the y direction is the individual monochromatic beam size. Unlike conventional imaging, wide-field imaging with SSTF allows for optical sectioning due to the evolution of the temporal pulse width within the sample, yielding the same axial confinement as conventional line-scanning imaging [12]. In SSTF line scanning, the beam at the back aperture is expanded in the y-dimension, yielding spatial focusing in the y dimension and temporal focusing in x. Thus, line-scanning SSTF has the same axial confinement as point-scanning MPM [12].

The experimental SFG SSTF setup is shown in Fig. 1. We use a mode-locked Ti:sapphire laser (Spectra-Physics Tsunami) centered at 744 nm with 14 nm of bandwidth (FWHM). A ruled diffraction grating with a 1200 lines/mm groove density separates the beam into its

monochromatic components, which are then collimated by a 40 cm focal-length lens and focused by an objective lens (Zeiss Fluar 20×/0.75 NA). We spectrally shape the beam by placing a metal rod (0.3cm hex key) at the input focal plane of the objective lens, blocking the center 7 nm (FWHM) of bandwidth. Note that the lateral spot size at the focus remains unchanged, because this is determined by the magnification of the individual monochromatic beams. Our sample is a thin film (~3 μm) of inhomogeneous Type I collagen on a #1 cover glass. The collagen film sample is prepared by drying a gel of bovine I collagen (Invitrogen). Loosely arranged Type I collagen has been shown to produce a significant amount of SHG in the backward direction [7, 24], facilitating imaging in the epidirection.

2.3 Experimental results

To observe the signal spectrum as a function of position, we use an optical fiber to collect the SFG signal into a spectrometer (Horiba SPEX 270M). We use an excitation spectrum centered at 800 nm owing to the sensitivity of the spectrometer. Figure 2.3 shows the resulting SFG spectrum versus the distance from the focus. The two outer peaks correspond to the SHG of the two excitation beams individually. The large central peak corresponds to the SFG of the two beams together. Note that the outer SHG peaks extend much further axially than the central SFG peak.

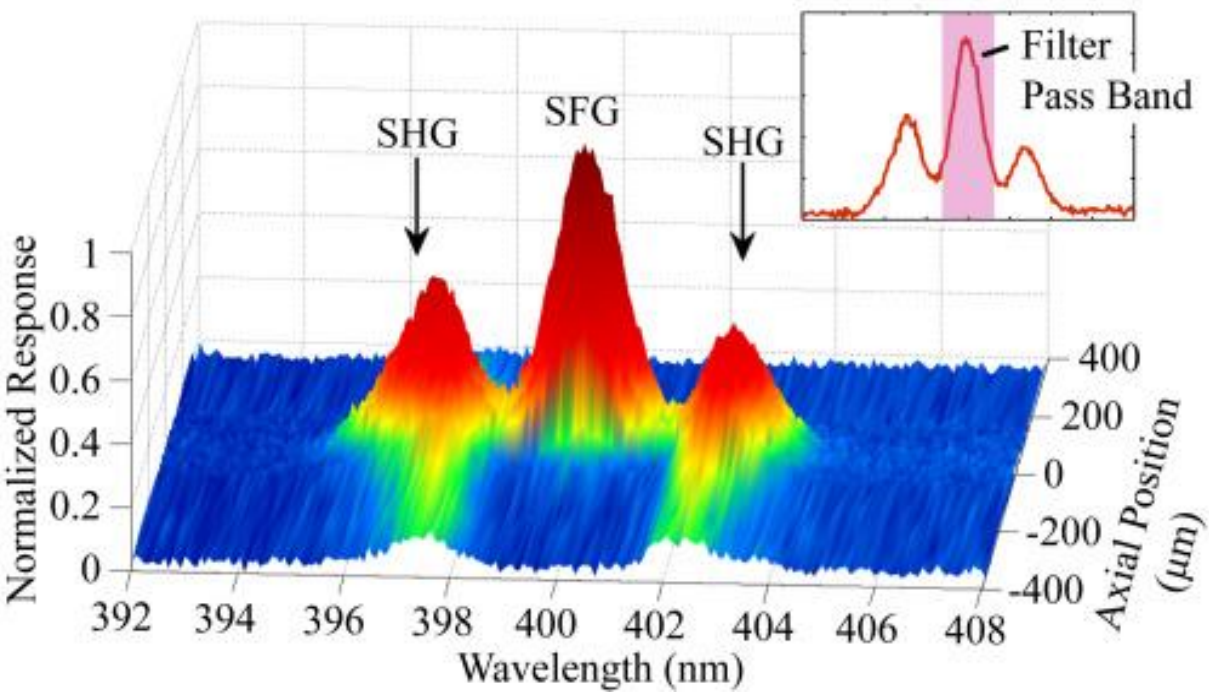

Figure 2.3: Measured spectrum as a function of axial position of a thin film of collagen.

Axial confinement is measured by scanning the collagen film through the focus on a translation stage (Figure 2.4). A narrow bandwidth (1 nm FWHM) emission filter (Semrock) centered at 372 nm selects the SFG from the focal region and rejects the SHG background. The signal is detected in the epidirection by a photomultiplier tube (PMT, Hamamatsu HC125-02). We perform these axial scans in both the wide-field and line-scanning SSTF configurations (squares in Figure 2.4 a, b respectively). We also compare the SSTF axial profile to that of a conventional SHG experiment with the same objective lens (triangles). Without spectral shaping, the SFG SSTF curves closely follow their corresponding SHG excitation profiles. With spectral shaping and filtering, the confinement improves in both wide-field and line-scanning SSTF, each to an improvement of 1 order of magnitude 30 μm from the focus (dark circles). Observe that the confinement is worse with the shaped spectrum but without the optical filter (light circles). This demonstrates that our effective pupil shaping is not the source of the enhanced confinement. We

note that in the wide-field SSTF configuration, the background-suppression technique significantly enhances the axial confinement and achieves performance similar to a conventional point-scanning system. In the line-scanning SSTF configuration, our technique significantly outperforms a conventional point-scanning system.

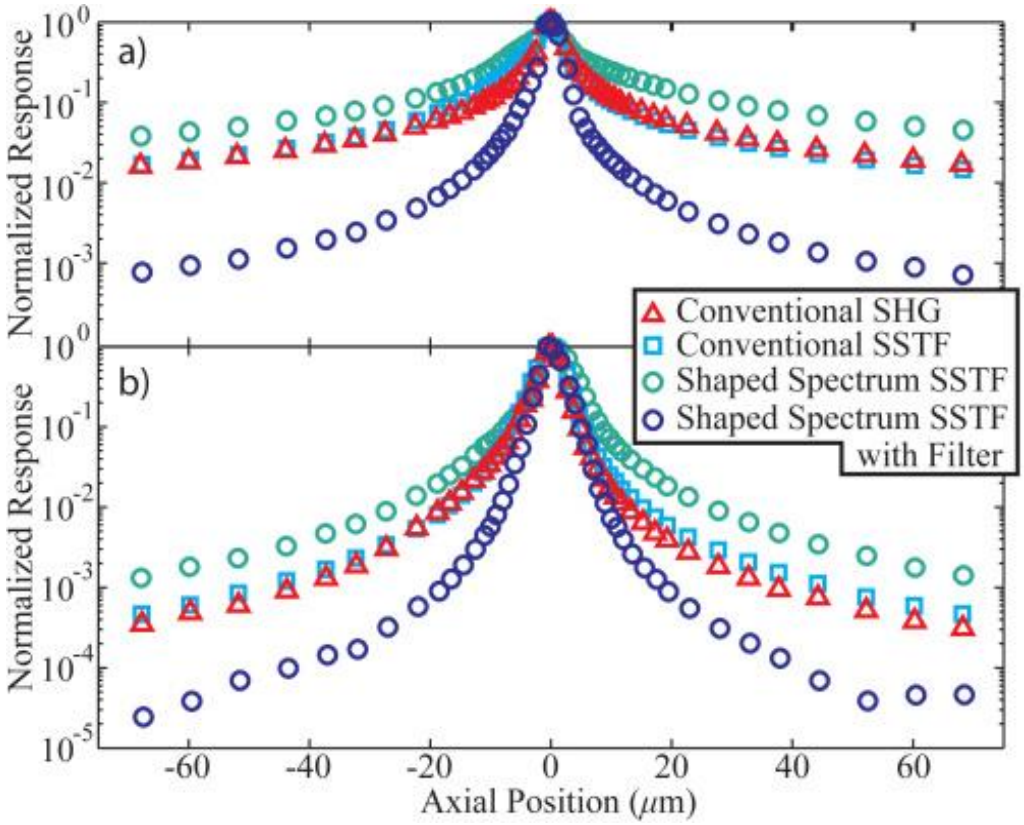

Figure 2.4: Measured thin film axial scans in the (a) wide-field and (b) line-scanning SSTF configurations

To demonstrate the utility of the enhanced axial confinement in the SFG SSTF technique, we prepare two thin collagen films separated by 45 μm. Keeping the narrow bandwidth filter in place, wide-field SSTF axial scans with and without spectral shaping are taken by sweeping the sample through the focus (Figure 2.5). Although the films are far apart (approximately ten times the axial FWHM), the poor axial confinement of standard wide-field SSTF yields a background

level of 7% in the overlapping region between the peaks. With a shaped spectrum, however, the two films are more clearly defined, and the background is reduced to 0.6% between the peaks. By simply adding a metal rod into the beam path, the axial confinement for wide-field SSTF is improved by 1 order of magnitude, achieving performance that is comparable to conventional point-scanning TPEF microscopy.

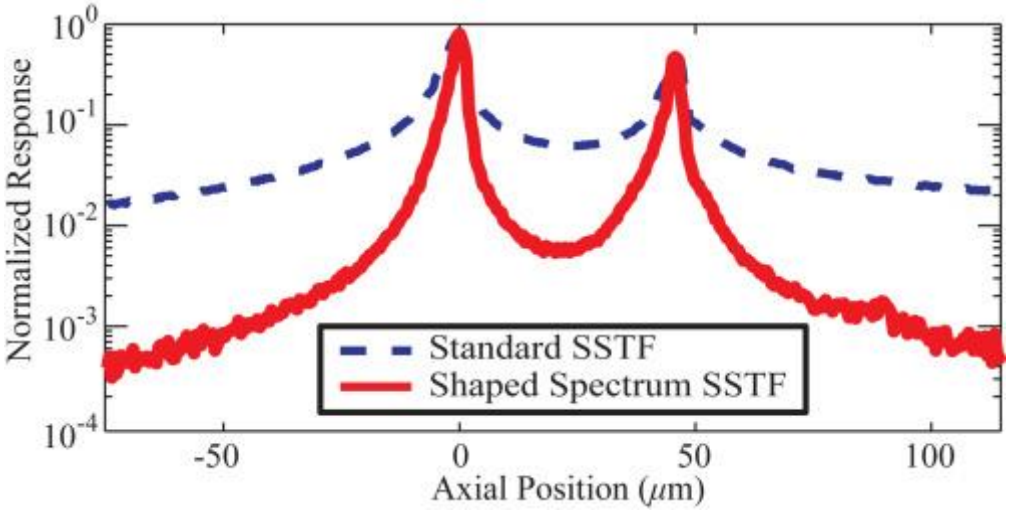

Figure 2.5: Measured axial response of two collagen films placed 45 μm apart, comparing standard SSTF to shaped spectrum SSTF.

There are many advantages to performing SFG in an SSTF setup. 2C2P microscopy typically requires two synchronized laser sources, whereas this technique requires only one. This requirement also eliminates the need for complicated delay lines and other sensitive alignment techniques in order to have the two "colors" spatially and temporally overlap at the focus. In addition, SSTF has the advantage of being able to scan the temporal focus axially by tuning the group-velocity dispersion [12]. Therefore this SFG technique combined with SSTF can yield a remote scanning-fiber probe with enhanced axial confinement and no moving parts at the distal end.

Because images in a wide-field or line-scanning SSTF setup must be captured with a camera, this technique has limited use when imaging deep into scattering tissue. At smaller depths or in non-scattering situations, however, wide-field SSTF can be valuable [25]. By incorporating our SFG SSTF technique, suppression of 1 order of magnitude of the out-of-focus background can be obtained at a distance as small as 30 μm away from the focus. Such a reduction in background is particularly valuable for wide-field SSTF, where the poor axial confinement is a major concern. A potential drawback of the proposed technique is that the distorted temporal profile of the pulse and the power loss due to the partial obstruction of the excitation beam make the SFG SSTF process inefficient. While sufficient signal can be generated by increasing the excitation power, there are more efficient approaches to shaping the spectrum of the excitation source. For example, it is well known that self-phase modulation can efficiently generate a spectrum with a central minimum without losing power or distorting the temporal intensity profile.

In summary, this technique demonstrates enhanced axial confinement by combining SFG with an SSTF setup, achieving a reduction of more than 1 order of magnitude of the out-of-focus background when compared with conventional TPEF microscopy. By rejecting the background in the optical domain using a narrowband optical filter (i.e., before the background photons reach the detector), this technique does not suffer noise problems common in other background subtraction techniques.

CHAPTER 3 :

HIGH SPEED MULTIPHOTON AXIAL SCANNING THROUGH AN OPTICAL FIBER IN A REMOTELY SCANNED TEMPORAL FOCUSING SETUP

3.1 Axial scanning in multiphoton systems

Scan speed is an important factor in *in vivo* microscopic imaging to reduce motion artifacts introduced by the sample movement. In a typical point-scanning depth-resolved microscope, the lateral dimensions are scanned using galvanometer mirror scanners at line rates of several kHz. Miniaturized MEMS scanners and piezo-electric scanners have been used for lateral scanning in miniature, flexible fiber probes [26, 27, 28]. The axial dimension in a typical microscope is scanned either by moving the sample relative to the output optics of the system or by moving a lens within the optical system. Because of the necessary movement of a bulk object, axial scanning is typically much slower than lateral scanning in a conventional microscope.

There are currently several techniques for higher speed depth-resolved axial scanning. For table-top multiphoton microscopy, a second, identical objective focused onto a small mirror may be placed optically conjugate to the main objective and sample. The mirror may be translated axially at high speed due to its small size, resulting in an axial scan of the focus on the sample [29]. Another method is to place a deformable mirror or spatial light modulator conjugate to the back focal plane of the imaging objective for arbitrary beam pointing and focusing [30]. These techniques are effective, although expensive and complicated. More importantly, since electronics and mechanical moving parts are required near the sample, they cannot be readily miniaturized or incorporated into a flexible fiber probe. While high speed axial scanning is routinely achieved in

optical coherence tomography (OCT) fiber probes [31], OCT does not provide the chemical specificity and spectral information offered by confocal and multiphoton techniques.

The temporal focus in a simultaneous spatial and temporal focusing (SSTF) setup can be remotely scanned by modulating the group delay dispersion (GDD) of the excitation pulse at the proximal end of a delivery fiber [12, 13, 14]. No moving parts or electronics are required at the distal end. However, previous demonstrations of axial scanning with SSTF are either at too slow a scanning speed or too small an axial scanning range for practical application. In Durst, *et. al.* [12], GDD tuning is achieved by moving bulk glass prisms on translation stages, severely limiting the maximum scanning speed. In Du, *et. al.* [32], acousto-optic deflectors are used to achieve high-speed GDD tuning. However, the small GDD tuning range limits the axial scanning range to only a small fraction of the axial resolution (i.e., axial full width half maximum). The technique described below presents high speed, chemically specific, large range axial scans of mouse tissue using GDD tuning in an SSTF setup. The technique is enabled by a novel dispersion modulation device based on a folded grating pair and a piezo-bimorph mirror. The large GDD tuning range (over $5x10^5$ fs^2) provided by the dispersion modulation device allows for a large axial scan range, with over 16 independently resolvable depth sections at a scan speed of 200Hz. The excitation pulses are delivered through a single-mode fiber, demonstrating the potential for future integration in a miniaturized fiber probe.

3.2 Group delay dispersion modulation with a piezo bimorph mirror

To effectively use SSTF in a GDD-tuned axial scanning setup, a method of modulating GDD over a large range at high speed is required. Typical methods for dispersion tuning include prism pairs and grating pairs [33, 34], but their tuning speed is limited by the mechanical

translation of these bulky optical elements. Electronically adjustable devices, such as acousto-optic modulators (AOMs) [35], spatial light modulators (SLMs) [36], and deformable mirrors [37, 38], can achieve programmable and high-speed dispersion tuning. These programmable devices can generate spectral phase of nearly arbitrary shape but at a high cost and with a limited GDD tuning range. In addition, their ability to generate higher-order dispersion is unnecessary, since tuning of the second-order group-delay dispersion is sufficient for remote axial scanning.

We demonstrate a GDD tuning device using a single piezo-bimorph mirror at the Fourier plane of a 4-f grating pair setup. Piezo bimorphs assume a quadratic shape with an applied voltage, allowing for large curvatures with high-speed electronic control [39, 40]. While pulse shaping using a piezo bimorph with multiple electrodes to independently address multiple sectors of the actuator has been demonstrated in the past [41], the use of a single piezo bimorph not only makes the device cost-effective but also provides large quadratic curvatures (i.e., GDD tuning range), avoiding both fabrication complexity and stroke limitations of multi-element deformable mirrors. The device is low cost, robust (high damage threshold), high speed, and has a large GDD tuning range of more than 10^5 fs^2 over a broad range of wavelengths.

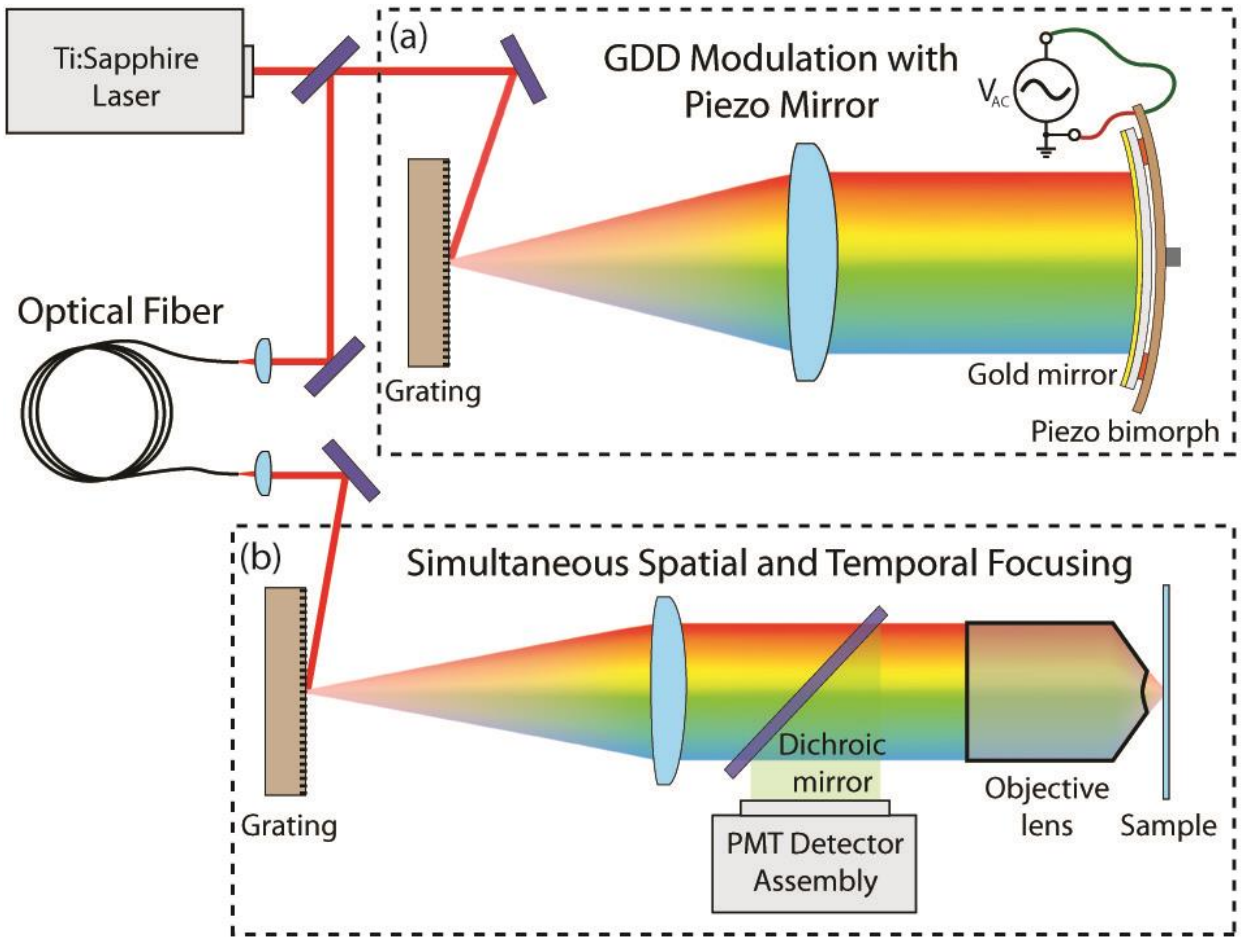

Figure 3.1: Experimental setup for remote axial scanning, including piezo-based GDD modulation and SSTF sample imaging.

The experimental setup of the GDD tuning device is shown in Figure 3.1 (a). A ruled diffraction grating (1800 lines/mm) spectrally separates the beam from a mode-locked Ti:Sapphire laser (λ_0 = 775 nm, $\Delta\lambda$ = 8 nm), which is then collimated by a spherical lens with a focal length of 30 cm. At the focal plane of the collimating lens, we place a piezo bimorph (T220-A4-503X, Piezo Systems, Inc.). The center of the piezo bimorph is fixed, allowing it to bend both forwards and backwards. A 380-micron thick pre-polished silicon wafer (University Wafer) is coated with gold to serve as a reflecting mirror, and it is mounted onto the piezo bimorph with double-sided Scotch

tape as spacers. The piezo bimorph is driven by a function generator combined with a linear amplifier. The bending of the piezo bimorph can be described by [39, 40, 42]:

$$y = -\frac{3d_{31}}{2T^2}Vx^2 \tag{3.1}$$

where y is the axial displacement of the piezo, x is the lateral position of the piezo with respect to the optical axis, V is the applied voltage, d_{31} is the piezoelectric coefficient, and T is the total thickness of the piezo. The difference in path length traveled by an individual monochromatic component is $2y$ due to the double pass configuration. The grating maps the individual frequency components, ω, to distinct lateral positions, such that for small spectral bandwidth, $x = \alpha_D\omega$. The quadratic path length difference is then mapped to quadratic spectral phase, or GDD:

$$2ky = \frac{1}{2}\mathrm{GDD}\omega^2 = \frac{1}{2}\mathrm{GDD}\left(\frac{x}{\alpha_D}\right)^2 \tag{3.2}$$

where k is the wavevector corresponding to the center wavelength λ_0. From Eqs. 4 and 5, the GDD at a driving voltage V is then:

$$\mathrm{GDD} = -\frac{12\pi}{\lambda_0}\frac{d_{31}\alpha_D^2}{T^2}V \tag{3.3}$$

Equation 3.3 shows that both normal and anomalous dispersions can be obtained in the same setup by changing the sign of the drive voltage. For example, for typical values V = 100 V, d_{31} = 1.9x10^{-10} m/V, T = 0.51 mm, α_D = 2.84x10^{-16} m/Hz, and λ_0 = 775 nm, the corresponding GDD will be 2.8x10^5 fs^2.

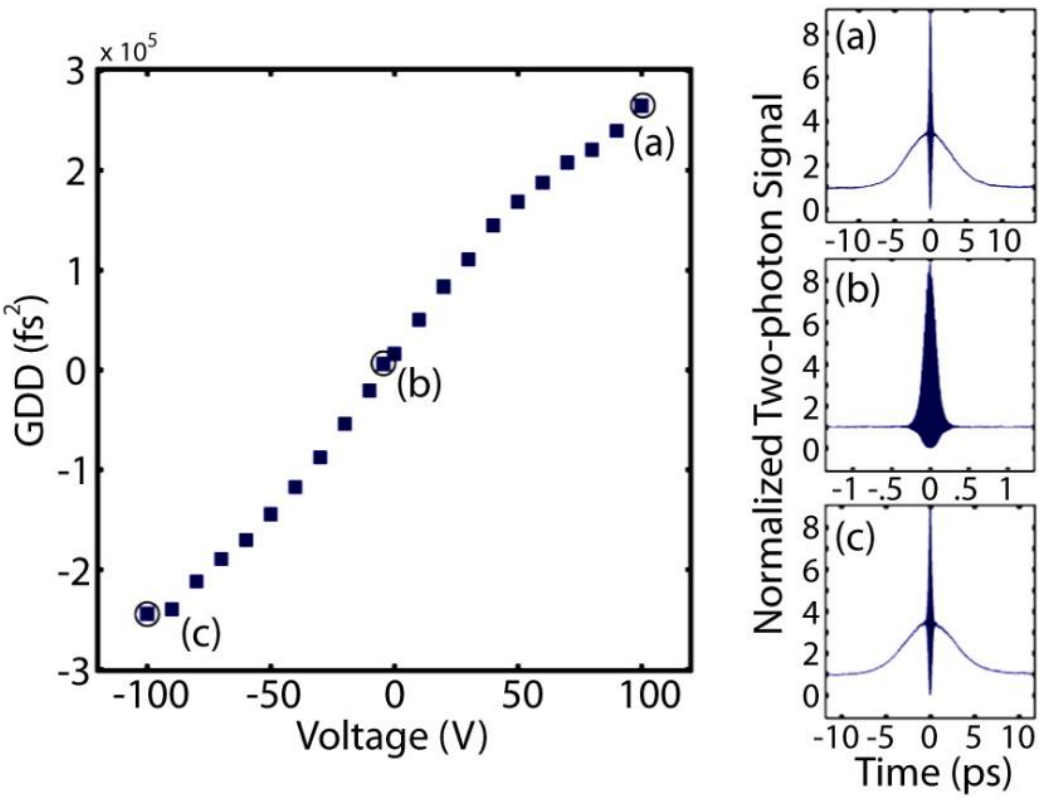

Figure 3.2: Measured GDD vs. piezo-drive voltage; second-order interferometric autocorrelation traces at -100V, 0V, and 100V.

To determine the GDD imposed on the pulse experimentally, the pulse width of the beam exiting the folded grating pair is measured using an interferometric second-order autocorrelator. The nonlinear element is a GaAsP photodiode. The beam is coupled out of the GDD device with a 50/50 beam splitter. A 100-fs pulse can be broadened to 4.2 ps by varying the drive voltage between +/-100V (Figure 3.2). Assuming a sech^2 shape of the spectrum, the piezo-bimorph mirror produces a GDD of $+/-2.5 \times 10^5$ fs^2, varying approximately linearly with voltage, and agreeing well with theory (Eq. 3.3). The device can be modulated at rates up to 100 Hz with no reduction in tuning range. The tuning range increases beyond 100 Hz as the piezo-bimorph mirror approaches its mechanical resonance (160 Hz), though it was not operated in this regime in order to prevent mechanical damage.

3.3 Axial scanning SSTF through a fiber

As described in chapter 1 section 2, the focal plane of a SSTF system may be axially scanned by altering the group delay dispersion, or GDD. The axial displacement is given by

$$\Delta z = \beta \Omega^2 \tag{3.4}$$

where β is the GDD and $\sqrt{2 \ln 2}\,\Omega$ is the FWHM of the excitation spectrum.

The GDD tuning device described in section 3.2 is used to perform remote axial scanning through a single mode fiber with SSTF. The experimental setup is shown in Figure 3.1. The Ti:Sapphire laser is tuned to 755nm with spectral bandwidth of 8.5nm (full width half maximum). After dispersion tuning the pulse is coupled into an air-core photonic bandgap fiber (Crystal Fibre, AIR-6-800), which has a nominal zero-dispersion wavelength of 754nm. An air-core fiber is used to avoid nonlinear effects during propagation. The output of the fiber is collimated and incident on a 1200 lines per mm diffraction grating at 65 degrees such that the first-order diffraction angle of the center wavelength is normal to the plane of the grating. The diffracted beam is collimated by a spherical lens with a 40-cm focal length, and refocused onto the sample with an objective lens.

Emission from the sample is reflected by a dichroic mirror and detected by a photomultiplier tube (PMT). A function generator provides a sinusoidal signal used to modulate the piezo-bimorph mirror and to provide a trigger for photon counting of the PMT signal. The PMT signal is then correlated with the piezo-drive voltage, which is proportional to the change of GDD in the system and thereby the axial displacement of the temporal focus (Eqs. 3.3 and 3.4). Because the temporal focus scans both forward and backward in one voltage cycle, the axial scan

rate is twice the modulation rate of the GDD. The triggering setup allows multiple axial scans to be averaged in real time to improve the signal-to-noise ratio.

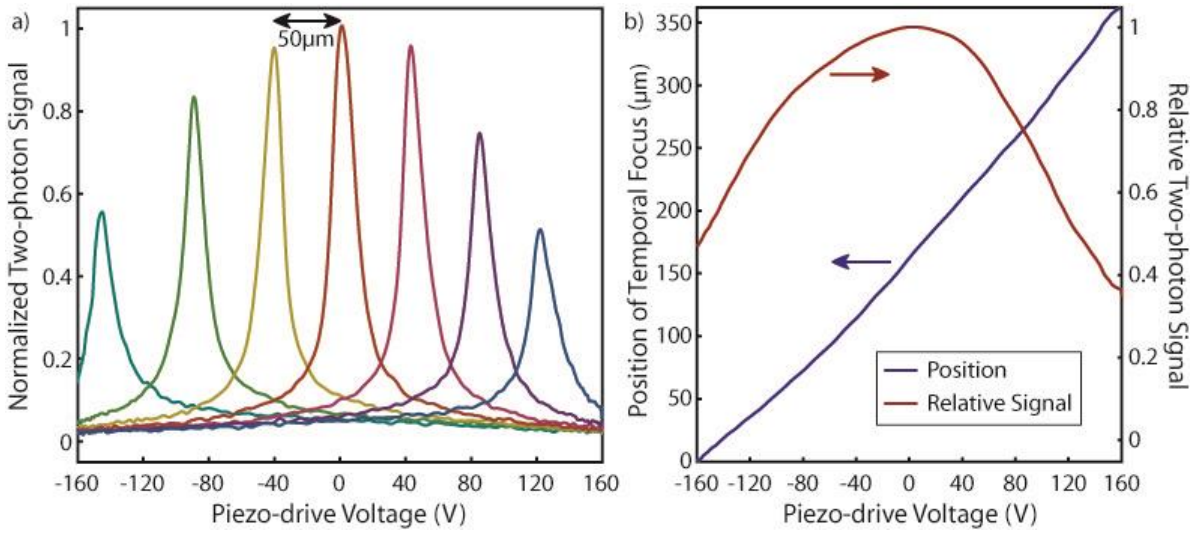

Figure 3.3: a) GDD axial scans of a Rhodamine B film of 0.5μm thickness. Two-photon fluorescence signal is plotted against the piezo-drive voltage. The film is moved 50μm between scans. b) Mapping of temporal focus position and relative two-photon signal strength to piezo-drive voltage.

A cover slip coated with a 0.5-micron film of fluorescent dye (Rhodamine B) is used as a test sample to calibrate the system. The sample is placed on a translation stage, and can be stepped axially through the temporal focus. The two-photon fluorescence signal is measured vs. the piezo-drive voltage for a number of fixed sample positions (Figure 3.3 a). Since the peak of each GDD scan corresponds to the sample position, the axial scan traces in Fig. 3 allow us to generate a mapping between the piezo-drive voltage and the position of the temporal focus setup (Figure 3.3 b). From this mapping we also extract the range and resolution of the remote scanning. We were able to extend the voltage range to +/-160V before two-photon signal strength dropped by more than a factor of two. This loss in signal is due largely to the range limit of remote axial scanning using SSTF, which was predicted in previous theoretical work [12], as well as variation in coupling

efficiency into the single-mode fiber, measured to have a root-mean-square variation of about 10% over this voltage range.

The data shown in Figure 3.3 was taken with an objective lens with a nominal focal length of 8 mm. The measured axial scan range is 360 μm with a resolution of 22 μm (FWHM). These results show that approximately 16 independently resolvable axial sections can be obtained in our setup. As shown in previous theoretical work, larger or smaller ranges, and correspondingly higher or lower resolutions, may be obtained by changing the focal length of the objective lens [12]. For example, with a nominally 18-mm focal length objective lens, we measure an axial scan range of 1450 μm with a resolution of 75 μm. With a nominally 3-mm focal length objective lens, we measure an axial scan range of 60 μm with a resolution of 3.8 μm.

To demonstrate feasibility in a biological sample, we perform axial scans of excised mouse skin. The multiphoton spectral signal of mouse skin is well characterized by Palero and Gerritson, *et. al.* [43]. The first fifteen to twenty microns of tissue comprise the epidermis, where multiphoton signal is dominated by intrinsic autofluorescence of cellular molecules, such as keratin and NADPH, in the 450 nm to 600 nm range. Beneath the epidermis is the dermis, which is primarily composed of structural proteins such as collagen and elastin fibers which give a strong second harmonic signal at one half the excitation wavelength (377.5 nm for excitation at 755 nm).

In this experiment we use a nominally 2.7-mm focal length water-immersion objective. The excitation wavelength is 755 nm and the pulse width is approximately 100 fs. The incident average power is 72 mW. We collect the signal with two separate PMT channels, one covering the 355 nm – 400 nm range targeting second harmonic generation, and the other covering the 500 nm – 650 nm range targeting autofluorescence. Remote axial scanning is performed by leaving the sample stationary and scanning the temporal focus by modulating the GDD. The thin film

characterization data is used to generate a position axis from the piezo-drive voltage and to correct for variations in the two-photon response at different positions of the temporal focus. For comparison, we also acquire an axial scan of the tissue by mechanically stepping the sample through a stationary temporal focus with a translation stage.

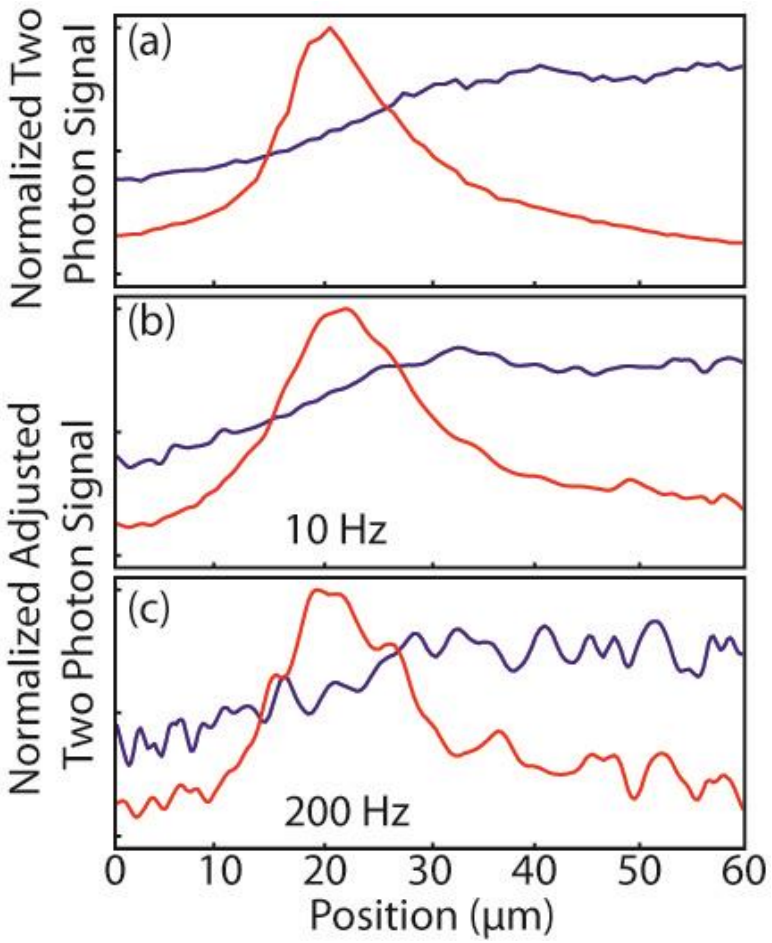

Figure 3.4: Axial scans of mouse skin. Axial scan taken by moving the sample through the temporal focus with a translation stage is shown in (a). Axial scans by GDD modulation at 10 Hz and 200 Hz are shown in (b) and (c). The 500 nm to 650 nm channel shown is in red. The peak is produced by autofluorescence in the epidermis. The 355 nm to 400 nm channel is shown in blue. The signal is strongest in the deeper, fibrous tissue of the dermis, producing second harmonic generation.

The results are shown in Figure 3.4. An axial scanning speed of 200 Hz is achieved, sufficient for overcoming motion artifacts for future *in vivo* imaging of live tissues. The epidermis

and dermis are clearly seen in the autofluorescence and second harmonic channels respectively, separated by about 20 microns. The GDD scans faithfully reproduce the stage scan, demonstrating that remote axial scanning using GDD tuning in an SSTF setup is equivalent to a mechanical sample scan.

3.4 Discussion and conclusion

In this experiment, the axial scan speed was limited to 200 Hz by the mechanical resonance of the piezo bimorph, measured to be 160 Hz (corresponding to an axial scan rate of 320 Hz). The resonant frequency can be increased significantly by reducing the size of the piezo-bimorph mirror, allowing for faster scan speeds. The ultimate limitation on the scan speed is imposed by the brightness of the sample, i.e., the desired signal-to-noise ratio of the axial scan trace. As shown in our results, an adequate signal-to-noise ratio can be obtained with an axial scan rate between 10 and 200 Hz.

Because a wide-field focus is necessary for SSTF to achieve a large axial scan range, the two-photon response is significantly smaller for a given excitation pulse than that for a conventional point focus. The reduction in signal generation rate is partially made up for by the increased integration time. A typical point-scanning system has a pixel dwell time on the order of 10 μs or less, whereas an SSTF system with 10 axially resolved points scanned at 100 Hz has a pixel dwell time of 1 ms, one hundred times larger. Additionally, because the focal spot in SSTF is much larger than that of a point focus, more excitation power may be delivered to the sample without causing nonlinear photodamage. Therefore, the average excitation power may be increased to further improve the signal-to-noise ratio of the axial scan. We note that one-photon absorption in the near IR (e.g., 800 nm) is typically small in biological samples. For example, optical trappings over

several seconds with approximately 100 mW average power are routinely used with minimal sample damage [44] [45]. In contrast, a tenth of a second or less is sufficient for one axial scan. In special circumstances where linear absorption is a concern, the signal-to-noise ratio can be improved by increasing the excitation pulse energy without increasing the average excitation power (i.e., by reducing the repetition rate).

The lateral width of the wide-field focus is dependent upon the spot size of the excitation beam on the diffraction grating and its demagnification onto the sample. A larger wide-field focus results in greater sample coverage and a longer available axial scan range, but results in decreased two-photon excitation. A smaller wide-field focus increases the two-photon excited signal over a narrower, more specific region of the sample, but reduces the available axial scan range before significant reduction in signal occurs. A more complete discussion of the impact of the lateral width can be found in Durst, *et. al.* [12]. In this experiment, the spot size on the diffraction grating was kept near 3 mm, resulting in wide-field foci of approximately 20 µm, 60 µm, and 140 µm on the sample for the objective lenses used. This choice is a trade-off between signal strength and the available axial scanning range.

The demonstrated remote axial scanning technique is best suited in a passive, flexible fiber probe for multiphoton excitation of axially resolved fluorescence and harmonic generation, bridging the gap between imaging optical endoscopes and non-imaging fiber optic probes. It has all the desirable attributes of a passive fiber probe but with added axial sectioning capability. As shown previously in depth-resolved tissue spectroscopy and imaging [5] [6] [7], the addition of axial sectioning to a conventional fiber probe will undoubtedly improve its diagnostic capability. The collection efficiency of such a probe can be enhanced through the use of large mode area or double-clad fibers [27], allowing for high collection efficiency throughout the depth of focus as

the focal plane is scanned. A dichroic mirror placed at an appropriate angle after the grating can redirect the two-photon signal into such a fiber without affecting the excitation beam.

In summary, high speed, large range, chemically specific multiphoton axial scanning of excised mouse skin through a single-mode fiber is demonstrated using SSTF. Because scanning is achieved by modulating GDD on the proximal end of the fiber, this technique may be implemented in a passive multiphoton fiber probe capable of producing high speed axial scans *in vivo* with no moving parts or electronics at the distal end. Such a remote scanning multiphoton probe can be an excellent compliment to existing OCT probes. An integrated SSTF and OCT passive fiber probe can be used to obtain both one-photon reflectance and two-photon fluorescence and harmonic generation signal, potentially enhancing its diagnostic capability.

CHAPTER 4 :

FREQUENCY MULTIPLEXED IN VIVO MULTIPHOTON PHOSPHORESCENCE LIFETIME MICROSCOPY

4.1 Phosphorescence lifetime imaging microscopy

Phosphorescence lifetime imaging microscopy (PLIM) [46] is a powerful technique for obtaining biologically relevant chemical information, e.g., through Förster resonance energy transfer and phosphorescence quenching [47, 48]. Point-measurement PLIM [49] of phosphorescence quenching probes has recently provided oxygen partial pressure measurements in small rodent brain vasculature identified by high-resolution MPM [50, 51]. However, the maximum fluorescence generation rate, which is inversely proportional to the phosphorescence lifetime, fundamentally limits PLIM pixel rates. Here we experimentally demonstrate a parallel-excitation/parallel-collection MPM-PLIM system that increases pixel rate by a factor of 100 over conventional MPM-PLIM while simultaneously acquiring lifetime and intensity images at depth *in vivo*. Full-frame three-dimensional *in vivo* PLIM imaging of phosphorescent quenching dye is presented for the first time and defines a new platform for biological and medical imaging.

Current technologies for overcoming the fundamental pixel rate limitation of serial-acquisition MPM require parallel excitation and imaging a sample onto multi-element detectors (typically CCD) [52, 53]. While satisfactory for thin tissue slices or non-scattering samples, thick scattering samples typically encountered in *in vivo* applications cause crosstalk between excited pixels when imaged onto a detector array, resulting in smeared images [54]. State-of-the-art fast fluorescence lifetime imaging microscopy systems utilize parallel excitation (e.g. LED arrays or pulsed diode excitation) or collection (e.g. gated CCD, single photon avalanche diode array, or

multichannel PMT) [55] for video rate acquisition [56, 57]. These systems have been applied to oxygen sensing [58, 59], but are similarly limited by excitation and emission crosstalk and cannot resolve 3D optical sections.

PLIM acquisition rates in phosphorescence quenching systems are further limited by long dye lifetime (T >1μs), which require low repetition rate lasers and long pixel dwell times (T>>s). Lifetime measurement rates of phosphorescent dyes often-used in oxygen sensing [48, 50, 51, 60, 61, 62], are thus limited to <10Hz at depth [51]. Although these systems provide valuable measurements at specific points within tissue (e.g. partial pressure of oxygen within specific vascular compartments), full-frame optical sectioning measurements of phosphorescent quenching at depth is impractical.

4.2 Lifetime measurement with multifocal multiphoton modulation microscopy

This chapter details a parallel-excitation/parallel-collection MPM-PLIM system that achieves high-pixel-rate, simultaneous lifetime and intensity imaging at depth *in vivo.* The basics of the technique are outlined in the introduction, chapter 1 section 3, describing multifocal multiphoton modulation microscopy (M4). Unlike prior parallel image acquisition approaches, does not require imaging of signal photons, thus eliminating the impact of signal scattering. Furthermore, in MPM, ballistic photons dominate the nonlinear excitation [63] until the imaging depth is many times the scattering length (e.g., ~ 1 mm in biological tissues) [64]; therefore, cross-talk from scattered excitation photons between neighboring pixels is eliminated.

In M4, each point in the sample is uniquely intensity modulated. The entire emitted signal is collected onto a single element detector. Spatial information is recovered via signal frequency

demodulation and pixel location is independent of sample-induced scattering. Each modulation frequency's magnitude and phase is mapped to fluorescence intensity and lifetime, respectively, for each pixel in the sample. Similar imaging techniques have been employed when detector arrays are impractical [65] and in fluorescence imaging [66, 67].

Assuming perfect sinusoidal modulation for simplicity, the modulated illumination excites a two-photon fluorescence response:

$$S(t) = \sum_i S_i \left(1 + \frac{4}{3\sqrt{1+(\omega_i\tau_i)^2}}\sin(\omega_i t + \theta_i) + \frac{1}{3\sqrt{1+(2\omega_i\tau_i)^2}}\sin(2\omega_i t + \varphi_i)\right) \quad (4.1)$$

where S_i is the cycle averaged signal strength; ω_i is the modulation angular frequency; θ_i and φ_i are, respectively, the phase delay due to the finite fluorescence lifetime (τ_i) at the fundamental modulation frequency ω_i and its second harmonic $2\omega_i$ at the i^{th}-pixel. All fundamental modulation frequencies (ω_i) are within a single octave to avoid crosstalk between the fundamental and second harmonic terms. Thus, the number of resolvable pixels is limited by the number of resolvable frequencies, given by $N = \frac{\omega_0}{2\pi}T$, where ω_0 is the lowest modulation frequency and T is the dwell time.

Complex demodulation of the emission signal yields the complete set of S_i and θ_i for all ω_i. The value of ω_i corresponds to the position of the i^{th}-pixel, while S_i gives the pixel intensity and θ_i can be used to calculate the fluorescence lifetime [46]:

$$\tau_i = \frac{\tan(\theta_i)}{\omega_i} \quad (4.2)$$

For optimum measurement of fluorescence lifetimes near τ_{target}, the angular modulation frequencies should be near $\omega_{\text{target}} = 2\pi\frac{0.1}{\tau_{\text{target}}}$ [68, 69]. M4 is capable of variable modulation

frequency to increase dynamic range. Furthermore, by restricting the modulation frequencies to one octave, the entire range of modulation frequencies across the sample is within the flat optimum in photon efficiency [68].

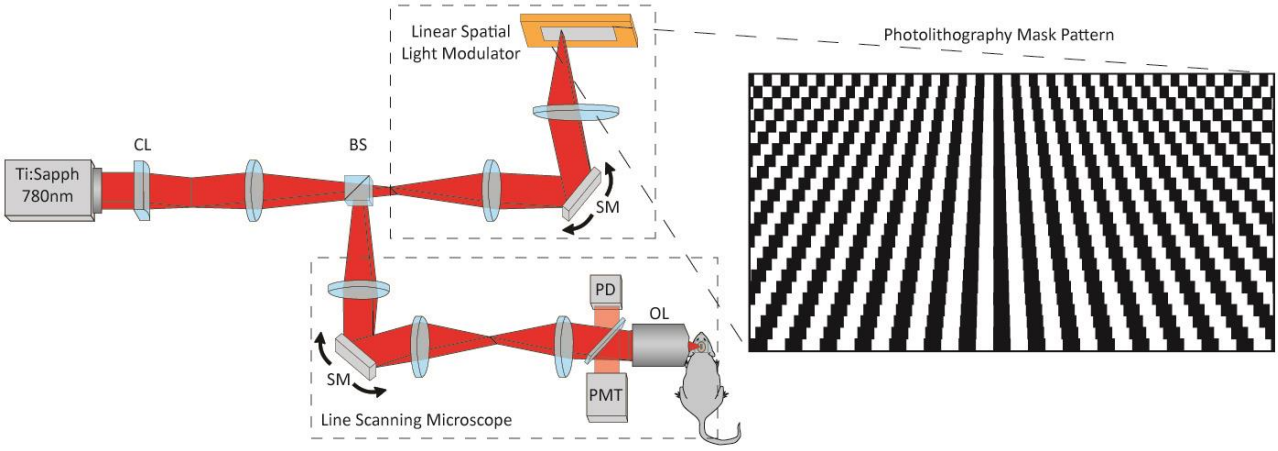

Figure 4.1: Schematic of the M4 microscope. CL, cylindrical lens; BS, beamsplitter; SM, scan mirror; PD, photodiode; PMT, photomultiplier tube; OL, objective lens. Right: illustration of the spatial light modulator, or SLM.

The experimental setup is described in Figure 4.1. A mode-locked Ti:sapphire laser was used as the excitation source (λ = 780 nm, pulsewidth ≈ 100 fs, repetition rate = 80 MHz, power in the range 80–150 mW at the sample). The beam is first focuse to a line using a 10 cm cylindrical lens. This line illumination then impinged onto a one-dimensional spatial light modulator (SLM), generating a linear array of point sources with each point source modulated by a different frequency (this process is described in Appendix 2, 'Custom reflection-based linear SLM' and the top dashed box in Figure 4.1). The linear point source array was imaged onto the sample to excite fluorescence, forming a one-to-one mapping between the modulation frequency and the pixel, that is, the spatial information along the focused line was encoded in the frequency domain by modulating the excitation light intensity. The excited nonlinear signal was epi-

collected through the objective and reflected off a dichroic mirror onto a large-area PMT (Hamamatsu H7422P-40). The dichroic mirror also reflected a small amount (<1%) of the 780 nm excitation light onto a silicon photodiode, which acted as a reference channel for fluorescence/phosphorescence lifetime measurements. The signal and reference channels were then processed as complex spectrograms to reconstruct, respectively, the reference and sample images. The modulation frequency was mapped to the *y*-axis, and time to the *x*-axis. The brightness of each pixel was determined by the magnitude measured in the signal spectrogram. The fluorescence/phosphorescence lifetime of each pixel was determined by the difference in measured phase between the signal and reference spectrograms. Data were collected on a 10 MHz National Instruments DAQ (PCI-6110) card and calculations were performed in real time in LabView (National Instruments Corporation). Post-processing and further data analysis were performed with custom scripts in MATLAB (Mathworks).

An intuitive analogy for this technique is subcarrier multiplexing, a standard communication technique. Each data channel is encoded in its distinct carrier radiofrequency (RF). A simple RF tuner then selects the desired band and filters out the rest. In the M4 PLIM system, each pixel in space acts like an independent data channel emitting at a distinct frequency that can be decoded to form a spatial image using the frequency-to-space correlation.

The M4 excitation and collection scheme is similar to that of line-scanning MPM. However, there is a significant difference in that each excitation point along the line is intensity-modulated at a unique frequency by a custom, reflection-based linear SLM capable of modulating up to ~1 MHz and corresponding to emission lifetimes of ~100 ns. For faster fluorescence lifetimes, commercially available polygon scan mirrors [70, 71] (SA24 & 72 sided polygon, Lincoln Laser) can further increase the modulation rates to 60 MHz, corresponding to a

lifetime resolution of ~50 ps and suitable for a wide range of biological fluorescent lifetime measurements. Alternatively, a two-dimensional digital micromirror device (DMD) or digital microelectromechanical system (MEMS) array can replace our linear SLM to achieve simultaneous full-field imaging by uniquely modulating and imaging a two-dimensional array of pixels onto the sample. Commercially available DMD kits (DLP4X00KIT, Texas Instruments) can already achieve 16 kHz modulation rates, suitable for wide-field M4 PLIM imaging of oxygen-sensing dyes.

An example of how M4 may be used to acquire intensity images is available in chapter 1, section 3, and in Figure 1.5. M4 axial and lateral resolution of two-photon excited fluorescence were measured by imaging 0.5μm diameter fluorescent (505/515) beads (Invitrogen) in a 3% agarose gel with a 0.75NA 20x objective. The lateral extent (FWHM) of the 0.5 μm bead was measured to be 1.13 μm and 0.73 μm along the frequency and time axes, respectively. The axial extent measured 4.0 μm. Lateral resolution along the frequency resolved dimension is limited by the demagnification of the modulator onto the sample.

Although multiplexing significantly increases the pixel rate of M4 versus serial point scanning PLIM systems, M4 suffers additional noise. Shot noise generated at a single pixel (i.e. modulation frequency) is shared among all simultaneously imaged pixels. Since two-photon eliminates cross-talk from the excitation and collection of photons, Shot noise is the dominant noise term. To address this concern, the microscope was adapted to perform both M4 and standard serial acquisition point scanning PLIM. $Ru(dpp_3)^{2+}$ [61] dyed tissue fibers were imaged using both techniques at equivalent sample illumination (i.e. equivalent fluorescence generation rate per pixel). This criterion was chosen since maximum fluorescence generation rate is the ultimate limitation on fluorescence imaging pixel rate for a large class of problems where the

generation rate of signal photons poses the fundamental limit to imaging speed. Therefore, the fair comparison is to excite samples in both systems close to the maximum generation rate and determine the relative error. The results shown in Figure 4.2 demonstrate two orders of magnitude improvement in pixel acquisition rate for M4 over point scanning MPM-PLIM.

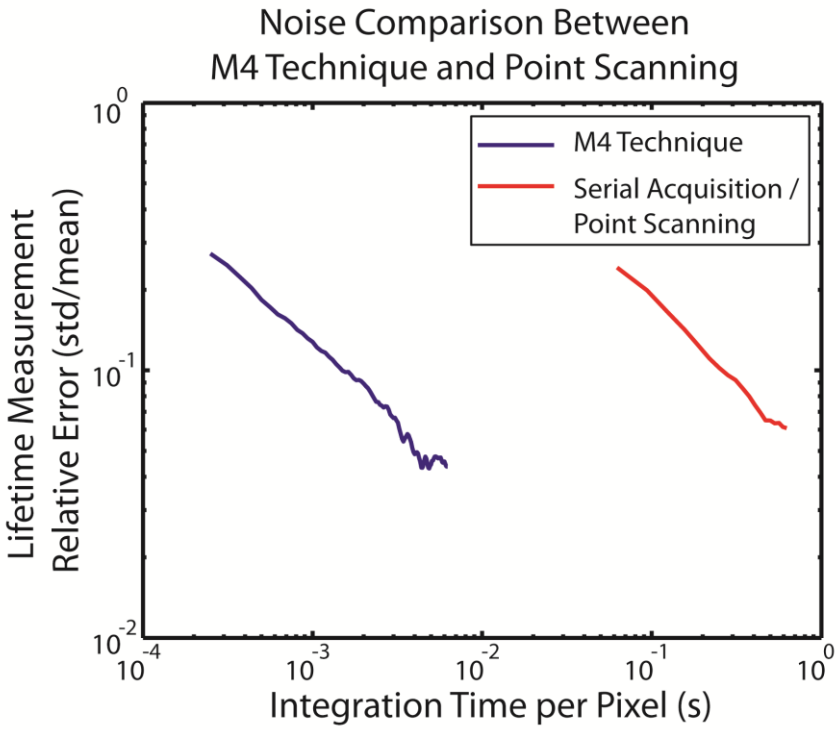

Figure 4.2: Noise comparison between M4 (blue) and Point Scanning (red), with relative lifetime measurement error plotted against integration time.

4.3 *In vivo* imaging of mouse brain

Significant interest exists in functional imaging of pO_2 in brain vasculature during stimulation [59, 72]. Recent work demonstrated functional imaging measurements at depth [51]. However, no oxygen sensing system produced 3D fluorescence/phosphorescence lifetime imaging of a heterogeneous lifetime system in a scattering medium (e.g., *in vivo).*

To demonstrate M4 *in vivo*, we injected Ru(dpp$_3$)-pluronic-nanomicelle probes into FVB/n mouse vasculature retro-orbitally. Optical access to the brain was achieved via a cranial window. Simultaneous intensity and lifetime optical sections are acquired by M4 (Figure 4.3). Blood vessels are clearly present in the intensity M4 image (Figure 4.3a), and phase is mapped to fluorescence lifetime with increasing averaging. Lifetime histograms of interior vascular compartments (800 pixels) displayed in Figure 4.3 (b-d) are presented in (e) from top to bottom, respectively. Image frames are 500x160 pixels with 85 mW optical power at the sample; the modulation rates range from 32-64 kHz. Figure 4.3f demonstrates simultaneous intensity and lifetime optical sections at 10 micron steps and 3 minute averaging per frame.

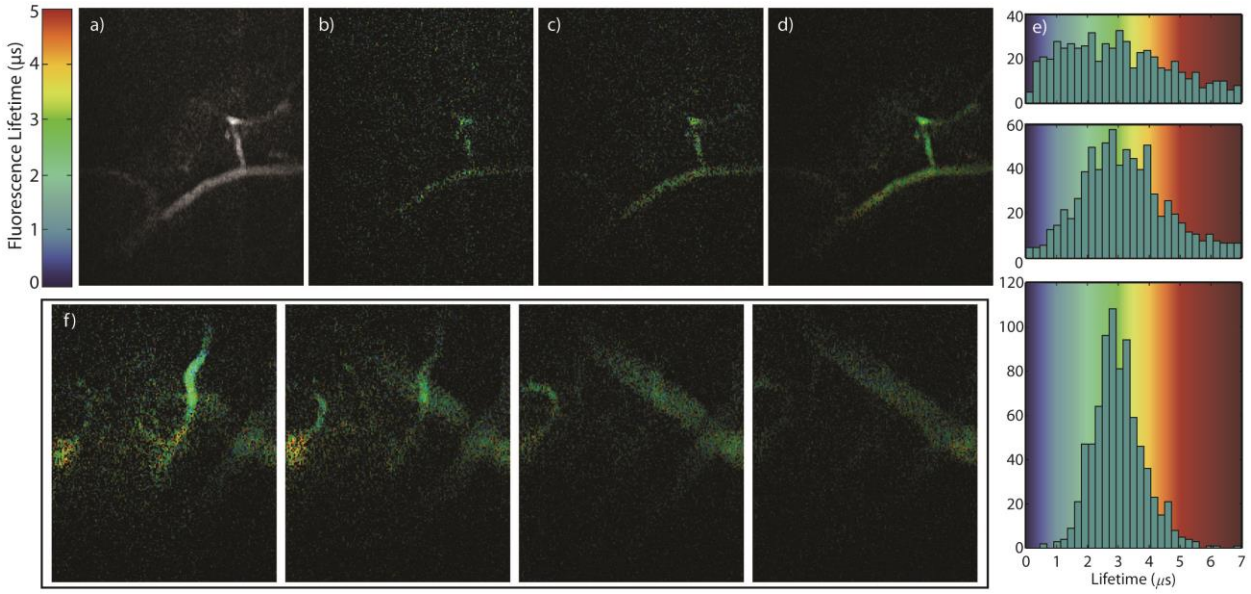

Figure 4.3: Mouse brain vasculature containing Ru(dpp$_3$)-pluronic-nanomicelle probes imaged by M4. **a**, Phosphorescence intensity. **b**–**d**, Phosphorescence lifetime after 20 s (**b**), 1 min (**c**) and 5 min (**d**) of integration. **e**, Top to bottom: lifetime histograms of 800 pixels from the interior of the blood vessel from images **b**–**d**, respectively. **f,** Optical sections separated by 10 µm through brain vasculature. Images **b**–**d** and **f** map lifetime to hue and intensity to value to simultaneously illustrate lifetime and intensity acquisition.

A heterogeneous *in vivo* sample was prepared by injecting Ru(dpp$_3$)-pluronic-nanomicelle probes into a fluorescent protein (DsRed) labeled mouse retro-orbitally.

Conventional two photon microscopy shows that DsRed is expressed predominately in the blood vessel walls in the absence of dye (Figure 4.4a). Optical sections of $Ru(dpp_3)$ in DsRed labeled mouse vasculature were obtained in 10 micron steps through a blood vessel. The simultaneously acquired intensity and lifetime images are presented in Figure 4.4 b and c, respectively. It is clear that the blood vessel walls contain fast lifetime ($\tau << 1$ μs) DsRed fluorescence while $Ru(dpp_3)$-nanomicelle dye (τ ~2.5μs) is localized in the vessel interior. The M4-PLIM optical stack of 11 full-frames through 110 μm is presented in Figure 4.4d, and represents, to our knowledge, the deepest *in vivo* PLIM imaging of phosphorescence quenching dye. The modulation frequencies are between 64 kHz and 128 kHz, the frame period is 3 minutes 20 seconds, and the average photon rate was less than 500 kHz (corresponding to a low photon generation rate per pixel of 1 kHz). The frame size is 256x500 pixels, yielding a PLIM pixel rate of 640 Hz. This is significantly faster than previously reported long lifetime two-photon PLIM imaging in a similar system (pixel rates of ~1 Hz [51]). M4 pixel rates can be greatly improved by increasing the photon generation rate with improved dyes or higher excitation pulse energy at sample.

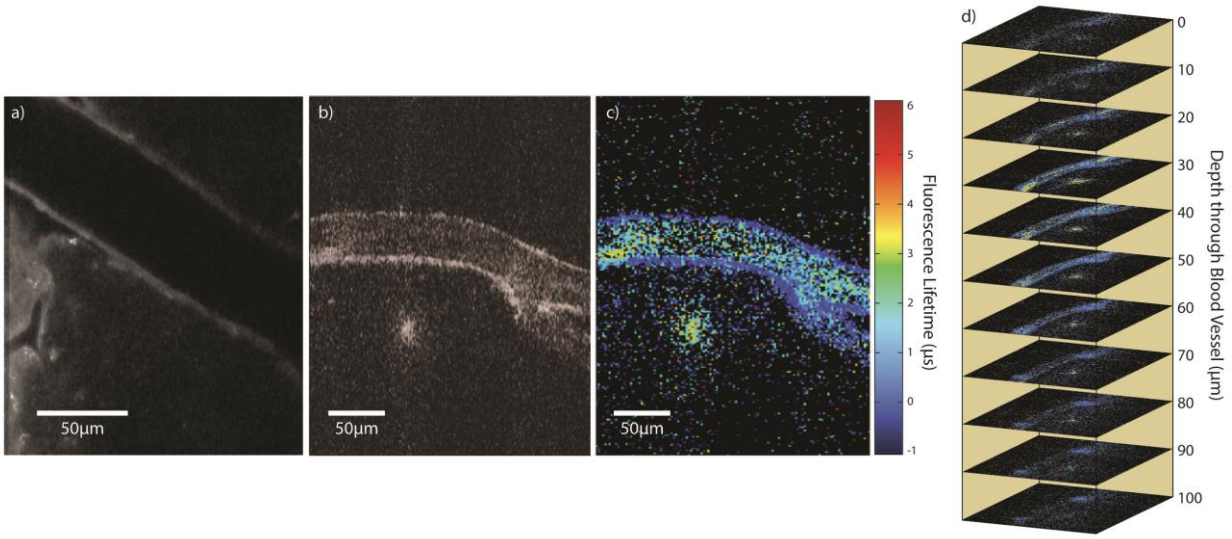

Figure 4.4: M4 and conventional two-photon microscopy of DsRed-labelled mouse brain vasculature, *in vivo*. **a**, Conventional point-scanning MPM of mouse-brain blood vessel labelled with DsRed, before $Ru(dpp_3)$ injection. **b**,**c**, M4 intensity (**b**) and lifetime (**c**) maps of DsRed-labelled mouse brain after injection of phosphorescent $Ru(dpp_3)^{2+}$ dye. **d**, Lifetime sections taken in 10 µm steps through the blood vessel after injection of $Ru(dpp_3)^{2+}$ dye.

In summary, we experimentally demonstrated a parallel-excitation/parallel-collection MPM-PLIM system that achieves high-pixel rate while simultaneously acquiring lifetime and intensity images at depth *in vivo*. By mapping spatial positions to modulation frequencies, image smearing due to signal scattering is avoided. M4 provides a two orders of magnitude improvement in pixel rate over serial acquisition PLIM, and allows, for the first time, full-frame three-dimensional lifetime imaging of a heterogeneous sample containing phosphorescence quenching probe.

CHAPTER 5 :

OVERVIEW OF SPEED LIMITATIONS IN MULTIPHOTON MICROSCOPY

4.1 Mechanical challenges and solutions for point-scanning microscopy

Conventional multi-photon microscopy is typically performed with two galvanometer mirrors. The simplest non-resonant setups have maximum scan speeds of 1 kHz or lower per galvanometer. For a 512 × 512 image, this limits the frame rate to about 4 fps. Resonant galvanometers reach speeds around 8 kHz, allowing for higher frame rates or higher resolution. Galvanometer bandwidth is largely limited by the size of the mirror, which must be large enough to reflect a laser beam of several millimeters diameter to reduce beam divergence angle.

Scanning in the axial dimension is typically performed by motorized or piezo-based stages, generally moving the entire sample or microscope head. Because they are moving such large masses, such stage-based axial scans are necessarily very slow. As such, typical MPM is limited to first scanning the entire XY plane before scanning axially. Higher axial scan speed similar to that achieved by mirror galvanometers can be achieved by mounting the objective lens on specialized piezo scanners designed for high load and high bandwidth [73]. Another technique is use a second objective focused onto a small, piezo-mounted mirror, optically conjugate to the sample [29]. Such techniques can reach axial scanning bandwidth of up to 1 kHz.

Alternative scanning systems that do not require the movement of bulk physical objects are required to significantly improve scan speed. In an acousto-optic deflector (AOD), a solid medium such as glass, quarts, or germanium is sandwiched between a piezo-electric transducer

and an acoustic absorber. The piezo generates an acoustic wave in the medium, forming a bragg grating via the acousto-optic effect. With a high enough center frequency (50-100 MHz), the acoustic wave can be frequency modulated with high bandwidth, deflecting the diffracted beam at varying angles at upwards of 10 MHz. In theory such high scan speeds would allow for high-resolution frame rates in excess of 10 kHz, though in practice sample brightness (and eventually detector bandwidth and laser repetition rate) impose stricter limitations. AODs have two major drawbacks compared to galvanometers: transmission and resolvable angles. Because AODs operate off of first order diffraction, their transmission is capped around 70% under ideal conditions, and generally 50% when scanning across the entire deflection range (compared to mirror galvanometers at over 97% transmission). Additionally, some form of spatial chirp compensation is required when using AODs with femtosecond pulses, further reducing transmission. Regarding resolution, limited aperture size and deflection range results in a maximum of 200 – 500 resolvable angles for most AODs on the market. Despite these drawbacks, the high bandwidth of AODs allows for so-called 'random-access' imaging, freely selecting points of interest within the sample at high speed [74].

Axial scanning can also be performed using AODs, albeit at great cost to transmission. Two optically conjugate AODs driven with chirped acoustic waves can focus or defocus a beam along the axis of deflection [75]. Two such pairs acting together can position an MPM focal volume at arbitrary points within a three-dimensional imaging volume at over 50 kHz, albeit with less than 5% laser power transmission [76]. Higher transmission fast axial scanning can be achieved with a tunable acousto-optic gradient index (TAG) lens, in which a cylindrical piezo-electric transducer drives a standing bessel acoustic wave within an acousto-optic medium [77]. Such systems can perform axial scanning at hundreds of kilohertz with near full optical

transmission. However, TAG lenses must be continually modulated at fixed resonant frequencies, and do not have the arbitrary pointing capability of AODs, representing significant practical difficulties in their use.

4.2 Laser power and repetition rate in point-scanning systems

When imaging at depth or without bright, highly concentrated dyes, multiphoton microscopy imaging speed is typically limited more by the brightness of the sample than by mechanical limitations imposed by point scanning. However, even with exceedingly bright samples or exceedingly powerful laser sources, limitations on the laser repetition rate (and therefore the pixel rate) are imposed by photo-damage, saturation, and sample heating.

Above one micron, ablative photo-damage occurs for femtosecond pulses above 15 nJ. Below this threshold, fluorescence saturation is generally achieved at around 1 nJ for two-photon imaging, and 5 nJ for three-photon imaging, representing the maximum useful pulse energy. Consider the goal of imaging a 1024 × 1024 pixel area with a three-photon microscope at video rate (30 fps). This would require a minimum repetition rate of 30×10^6 pulses per second. At 5 nJ per pulse, this is a minimum average power of 150 mW (and at least 500 mW at the laser source before transmission losses through the microscope). This is already well above the thermal power limit for 1700 nm excitation in mouse brain (~40 mW), and close to the limit for lower wavelengths. For deep tissue imaging, considerably more power is required to account for the scattering length of the tissue, further increasing the thermal load and demands upon the laser source. Optimal laser repetition rates to avoid tissue damage for two- and three-photon deep tissue imaging are around 5 MHz and 1 MHz respectively (5 fps and 1 fps respectively for a

1024 × 1024 image, or 20 fps and 4 fps for a 512 × 512 image). Significantly faster sources are appropriate for imaging within the first scattering length, at the cost of depth penetration.

4.3 Parallel imaging and frame rate

Wide-field illumination and parallel pixel acquisition removes the mechanical limitations of point scanning microscopy, but introduces other problems. High speed EMCCDs or Scientific CMOS cameras can achieve pixel readout rates of over 500 MHz (500 frames per second at 1024 × 1024 pixels, or 2000 fps at 512 × 512). However, use of a camera requires faithful imaging of points within the focal plane onto the micron-scale pixels of the camera itself, whereas a time-gated single-element detector such as a PMT only requires imaging onto a centimeter-scale target. Consequently, cameras can only be used when tissue scattering is minimal, generally within the first 150 - 200 microns of a biological sample [78].

Regarding laser power and illumination, wide-field imaging requires much higher pulse energy to achieve the same nonlinearity across a large area. Consider imaging a 250μm × 250μm area with wide-field excitation. While a raster scanning microscope would require a 1 nJ pulse suitable for excitation of a 0.5μm × 0.5μm pixel, the wide-field imaging microscope requires a pulse energy 250,000 times higher (250 μJ) to achieve the equivalent nonlinear excitation over the full area. Highly energetic pulses can be generated with regeneratively amplified sources, and have been used in conjunction with cameras to achieve multi-photon frame rates in excess of 100 fps [79, 78]. The repetition rate of such sources is far lower than those used for point-scanning microscopy, although parallel pixel acquisition makes up the difference in imaging speed. Note that the repetition rate of the laser source represents an upper bound to the frame rate. Such high

pulse energies represent significant challenges both in generation and propagation. For many such applications, less-than-ideal pulse energies at higher repetition rates will be more practical at a sacrifice to photon efficiency. Assuming appropriate low duty-cycle pulsed sources (a big assumption), wide-field imaging is identical to point scanning with appropriately fast scanners. The advantage to wide-field parallel imaging is that complicated scanning techniques are not required, at the cost of axial confinement and image blur in thick scattering samples.

Parallel pixel imaging can also be performed with a single-element detector, such as in the multifocal multiphoton modulation microscopy (M4) technique described in Chapter 4. This and other multifocal techniques blur the line between spatial and temporal distinctions between pixels, achieving greater axial confinement and imaging depth than wide-field imaging but suffering greater noise concerns than traditional point-scanning microscopy. Such techniques can achieve faster imaging speeds than traditional microscopy for certain samples, namely those with high-contrast, sparsely-populated images. Further discussion of such techniques is available in Chapter 4 and in Appendix B.

APPENDIX A :

PHYSICAL PARAMETERS IN TEMPORAL FOCUSING SETUPS

When designing temporal focusing setups, the two most important spatial design parameters are field of view and axial confinement. As temporal focusing setups consist of a diffraction grating imaged onto the sample, the field of view is simply the beam size on the diffraction grating divided by the demagnification of the optical system. However, the axial confinement of the resulting focal volume is less obvious. The clearest equation available in current literature is given by Durst et. al. [12] for the axial full width at half maximum (AFWHM):

$$\text{AFWHM} = 2\sqrt{3}\frac{2f^2}{k\,(s^2 + \alpha^2\Omega^2)} \tag{A.1}$$

where f is the focal length of the objective lens, k is the magnitude of the wavevector, and s and $\alpha\Omega$ are the monochromatic spot size and full-spectrum width of the excitation beam at the back focal plane of the objective lens, respectively. For most temporal focusing systems, the value $\alpha\Omega$ will be much larger than s, simplifying equation A.1 to

$$\text{AFWHM} = 2\sqrt{3}\frac{2f^2}{k\,\alpha^2\Omega^2} \tag{A.2}$$

The values of f and $\alpha\Omega$ are awkward design parameters to work with, but can be related simply to physical parameters such as the line density of the grating, the bandwidth of the excitation spectrum, and the magnification of the optical system (result at equation A.8).

The value of $\alpha\Omega$ is a function of the angle of diffraction off of the diffraction grating and the focal length of the collimating lens:

$$\alpha\Omega = f_c\left(\tan\left(\theta_{\lambda_2}\right) - \tan\left(\theta_{\lambda_1}\right)\right) \tag{A.3}$$

In a temporal focusing setup, the angle of diffraction for the central wavelength is zero. Starting from the grating equation:

$$\sin(\theta_i) + \sin(\theta_m) = \frac{m\lambda}{d} \tag{A.4}$$

where θ_i is the angle of incidence, θ_m is the angle of diffraction, m is the order of diffraction, λ is the wavelength and *d* is the line width of the grating. Since θ_m is zero at the center wavelength and we are interested in the first order diffraction (m = 1), equation A.4 reduces to:

$$\frac{\lambda_c}{d} + \sin(\theta_m) = \frac{\lambda}{d} \tag{A.5}$$

where λ_c is the central wavelength. Rearranging and using the small angle approximation, we find:

$$\tan(\theta) \approx \sin(\theta) = \frac{\lambda_c - \lambda}{d} \tag{A.6}$$

Plugging into equation A.3, and with the definition $\lambda_2 - \lambda_1 = \Delta\lambda$ we find the very simple result:

$$\alpha\Omega = \frac{\Delta\lambda}{d} f_c$$

where *d* is the line spacing of the grating, f_c is the focal length of the collimating lens, and $\sqrt{2\ln(2)}\,\Delta\lambda$ is the full width half maximum of the spectrum (see Durst et. al. [12]). Putting this back into equation A.2, we find:

$$\text{AFWHM} = \frac{4\sqrt{3}}{k} \frac{d^2}{\Delta\lambda^2} \frac{f^2}{f_c^2} \tag{A.7}$$

The ratio of the focal length of the objective lens *f* to the focal length of the collimating lens f_c is simply the magnification of the system, *M*, resulting in the very simple result:

$$\text{AFWHM} = \frac{4\sqrt{3}}{k} \frac{d^2}{\Delta\lambda^2} M^2 \tag{A.8}$$

From this result it is clear that tightest axial confinement is achieved with high line density on the grating (low d), a large spectral bandwidth (high $\Delta\lambda$), and a large magnification factor between the sample and the grating. Note that may require a large spot size on the grating to achieve a reasonable field of view. Such a system maximize both the area and angular divergence of the optical system at the grating (i.e. high etendue).

+

APPENDIX B :

NOISE ANALYSIS OF FREQUENCY MULTIPLEXED MULTIPHOTON MICROSCOPY

B.1 Frequency domain FLIM:

A thorough theoretical treatment of conventional frequency domain FLIM is given by J. Phillip and K. Carlsson [68]. In frequency domain FLIM, the excitation light for a fluorophore is modulated at a frequency on the order of the inverse of the fluorescence lifetime. The finite lifetime of the fluorophore has two effects on the measured fluorescence emission. First, the emission exhibits a lifetime-dependent phase delay relative to the excitation. Second, the finite fluorescence lifetime introduces a "smoothing" effect to the emission signal, causing a reduction in depth-of-modulation relative to the excitation. Assume a perfect sinusoidally modulated excitation given by,

$$I(t) = I_0\big(1 + M_E \sin(\omega t)\big) \tag{B.1}$$

where I_0 is the average excitation intensity, M_E is the modulation depth, and ω is the angular modulation frequency. The resulting detected fluorescence emission signal will be,

$$F(t) = F_0\big(1 + M_F \sin(\omega t + \phi)\big) \tag{B.2}$$

where F_0 is the average detected fluorescence signal and M_F is the fluorescence emission modulation depth. The phase delay ϕ is dependent upon the fluorescence lifetime and the modulation rate, and once measured can be used to make fluorescence lifetime measurements:

$$\tau = \frac{\tan(\phi)}{\omega} \tag{B.3}$$

The depth of modulation in the fluorescence signal will always be less than that of the original excitation due to the smoothing effects of the finite fluorescent lifetime. The ratio between the two is given by:

$$\frac{M_F}{M_E} = \frac{1}{\sqrt{1+(\omega\tau)^2}} \tag{B.4}$$

The angular modulation frequency, ω, should be chosen carefully to maximize the signal-to-noise ratio of the lifetime measurement. Error analysis of equation B.3 shows that the error in the lifetime measurement is given by

$$\Delta\tau \approx \frac{\sec^2(\phi)}{\omega}\Delta\phi = \frac{1+(\omega\tau)^2}{\omega}\Delta\phi \tag{B.5}$$

where $\Delta\phi$ is the error in the measurement of ϕ and it is assumed that $\Delta\omega$, the error in ω, is negligible. The prefactor $\frac{1+(\omega\tau)^2}{\omega}$ reaches a minimum at $\omega = \frac{1}{\tau}$. However, the accuracy of the phase delay measurement, $\Delta\phi$, is dependent upon the depth of modulation of the emission signal and is improved with decreasing ω. This pushes the optimal modulation frequency considerably lower than $\omega = \frac{1}{\tau}$. Theoretical work by J. Phillip and K. Carlsson [68] shows the optimal modulation frequency to be around $f = \frac{\omega}{2\pi} = \frac{0.1}{\tau}$.

B.2 Comparison of Signal-to-Noise Ratio for M4 and Conventional FLIM

We now compare the signal-to-noise ratio for M4 as compared to conventional frequency domain FLIM. We assume sinusoidal excitation modulation. For conventional frequency domain FLIM, the total number of useful collected signal photons for a fluorescence lifetime measurement of the *n*th pixel in an image is given by

$$S_{n,\,\mathrm{FLIM}} = M_{F,n}\, g_n T_{\mathrm{FLIM}} \tag{B.6}$$

where $M_{F,n}$ is the fractional depth of modulation of the measured emission, g_n is the mean photon generation rate, and T_{FLIM} is the pixel dwell time for the FLIM system. The inherent shot noise in the measurement is the square root of the total number of collected photons:

$$N_{n,\,\mathrm{FLIM}} = \sqrt{g_n T_{\mathrm{FLIM}}} \tag{B.7}$$

The photon signal-to-noise ratio for a given pixel is then given by:

$$\mathrm{SNR}_{n,\ \mathrm{FLIM}} = \frac{S_{n,\,\mathrm{FLIM}}}{N_{n,\,\mathrm{FLIM}}} = M_{F,n}\sqrt{g_n T_{\mathrm{FLIM}}} \tag{B.8}$$

For the M4 technique, the analysis is similar. The total number of useful collected photons for a fluorescence lifetime measurement of the *n*th pixel in an image is given by

$$S_{n,\,\mathrm{M4}} = M_{F,n}\, g_n\, N\, T_{\mathrm{M4}} \tag{B.9}$$

where N is the number of pixels in a line and the product $N\, T_{\mathrm{M4}}$ is the pixel dwell time for the M4 system. The shot noise in the measurement is the total number of collected photons during this interval. This includes photons generated by all N pixels:

$$N_{n,\,\mathrm{M4}} = \sqrt{\sum_m (g_m N\, T_{\mathrm{M4}})} = N\sqrt{g_{\mathrm{ave}} T_{\mathrm{M4}}} \tag{B.10}$$

Here $g_{\mathrm{ave}} = \frac{\sum g_m}{N}$ is the average photon generation rate for the line. Note that the shot noise for each pixel in a line is the same. The resulting signal-to-noise ratio is then given by:

$$\mathrm{SNR}_{n,\ \mathrm{M4}} = \frac{S_{n,\,\mathrm{M4}}}{N_{n,\,\mathrm{M4}}} = M_{F,n}\frac{g_n}{\sqrt{g_{\mathrm{ave}}}}\sqrt{T_{\mathrm{M4}}} \tag{B.11}$$

To compare the M4 technique with conventional FLIM, we look at the ratio of their SNRs for a given pixel:

$$\frac{\mathrm{SNR}_{n,\ \mathrm{M4}}}{\mathrm{SNR}_{n,\ \mathrm{FLIM}}} = \sqrt{\frac{g_n}{g_{\mathrm{ave}}}\frac{T_{\mathrm{M4}}}{T_{\mathrm{FLIM}}}} \tag{B.12}$$

A second useful way to compare the two techniques is to recognize that the inverses of T_{M4} and T_{FLIM} are the pixel rates for the M4 and FLIM techniques respectively. Defining $R_{\mathrm{M4}} = \frac{1}{T_{\mathrm{M4}}}$ and $R_{\mathrm{FLIM}} = \frac{1}{T_{\mathrm{FLIM}}}$, we calculate the ratio of the pixel rates for the two techniques:

$$\frac{R_{\mathrm{M4}}}{R_{\mathrm{FLIM}}} = \frac{g_n}{g_{\mathrm{ave}}}\left(\frac{\mathrm{SNR}_{n,\ \mathrm{FLIM}}}{\mathrm{SNR}_{n,\ \mathrm{M4}}}\right)^2 \tag{B.13}$$

From equations B.12 and B.13 we see that for a direct comparison of lifetime measurements between the two techniques at a constant pixel rate ($T_{\mathrm{M4}} = T_{\mathrm{FLIM}}$), the ratio in SNR has square root dependence on pixel brightness, and for a comparison at a constant SNR ($\mathrm{SNR}_{n,\ \mathrm{M4}} = \mathrm{SNR}_{n,\ \mathrm{FLIM}}$), the ratio in pixel rate has a linear dependence on pixel brightness. Here, "brightness" is defined relative to the average pixel brightness along a given line in the image. For a pixel of average brightness (g_n=g_{ave}), the two techniques perform equally. For brighter than average pixels, the M4 technique has a corresponding SNR or pixel rate advantage, while the reverse is true for dimmer than average pixels.

In many samples of interest, the fluorescent dyes targeting specific biological structures are present in only a small fraction of the entire field of view. If the majority of pixels are do not contain dye, they will be dark and the average pixel brightness will be very low. Consequently, the relative brightness of dye-containing pixels of interest will be very high, a regime in which the M4 technique significantly outperforms conventional FLIM.

B.3 Intensity measurement

The treatment of signal-to-noise for the M4 technique when making intensity measurements is similar, though modulation depth of the signal plays a larger role. We find the same SNR for M4 as equation B.11:

$$\mathrm{SNR}_{n,\ \mathrm{M4}} = \frac{S_{n,\,\mathrm{M4}}}{N_{n,\,\mathrm{M4}}} = M_{F,n}\frac{g_n}{\sqrt{g_{\mathrm{ave}}}}\sqrt{T_{\mathrm{M4}}} \tag{B.14}$$

FLIM doesn't include modulation depth, as all photons are known to come from the pixel:

$$\mathrm{SNR}_{n,\ \mathrm{FLIM}} = \frac{S_{n,\,\mathrm{FLIM}}}{N_{n,\,\mathrm{FLIM}}} = \sqrt{g_n T_{\mathrm{FLIM}}} \tag{B.15}$$

The ratios of SNR and pixel rate then become:

$$\begin{aligned} \frac{\mathrm{SNR}_{n,\ \mathrm{M4}}}{\mathrm{SNR}_{n,\ \mathrm{FLIM}}} &= M_{F,n}\sqrt{\frac{g_n}{g_{\mathrm{ave}}}\frac{T_{\mathrm{M4}}}{T_{\mathrm{FLIM}}}} \\ \frac{R_{\mathrm{M4}}}{R_{\mathrm{FLIM}}} &= \frac{g_n}{g_{\mathrm{ave}}}\left(M_{F,n}\frac{\mathrm{SNR}_{n,\ \mathrm{FLIM}}}{\mathrm{SNR}_{n,\ \mathrm{M4}}}\right)^2 \end{aligned} \tag{B.16}$$

B.4 Improving SNR by filtering dim pixels:

For "dark" pixels in which $g_n \ll g_{\mathrm{ave}}$, shot noise will dominate the measurement. Because shot noise is random, it is possible that the measured phase delay will lie outside of the $0^{\mathrm{o}} \le \phi < 90^{\mathrm{o}}$ range which results in real and positive fluorescence lifetime measurements. A completely dark pixel contributing zero signal photons to the image will have a 75% chance of

measuring an unphysical lifetime. This unphysical lifetime indicates that the majority of pixel brightness is due to shot noise, and the pixel brightness may then be reduced in post-processing.

APPENDIX C :

MULTIFOCAL MULTIPHOTON MODULATION MICROSCOPY METHODS

C.1 Custom Reflection Based Linear Spatial Light Modulator:

High modulation rates are required (e.g., ~ 100 kHz used in our experiments) to resolve distinct points along the line and to optimally match the desired fluorescence/phosphorescence lifetime. Since commercially available linear SLMs with the required pixel numbers cannot modulate at such high speeds, we created a free-space optical chopper (Figure 4.1a, dashed box) that can modulate an array of point sources at MHz rates by scanning a line-focused laser beam over a small (10-20 μm period) mirror grating on a photolithography mask (Figure 4.1b). Each horizontal line on the photolithography mask has a different spatial frequency. The reflected light is then descanned by the same scan mirror, and is imaged onto the sample by the line scanning microscope. The spatial frequencies are limited to one octave to avoid crosstalk between the fundamental modulation frequency and higher harmonics generated by the nonlinear response of the dye and deviations from a perfect sinusoidal modulation.

C.2 Serial Acquisition Two Photon PLIM Microscope:

A serial acquisition frequency domain PLIM microscope was built to compare the pixel rate improvement of M4 over serial acquisition PLIM microscopy. The same M4 microscope described in Methods is used for both parallel and serial acquisition. The microscope is modified for serial acquisition by removing the first cylindrical lens. A conventional point focus is then

obtained on both the sample and spatial light modulator. The spatial light modulator thus acts as an optical chopper and intensity modulates the excitation beam. The input optical power is adjusted so that the excitation intensity at the sample is identical in both parallel and serial acquisition.

The pixel rate comparison was performed by measuring the relative lifetime uncertainty of identical regions of an $Ru(dpp_3)$ dyed lens-paper with both M4 and serial point scanning MPM-PLIM in the frequency domain as a function of pixel dwell time.

C.3 Lifetime measurement calibration:

The lifetime measurements were calibrated by measuring the phase delay of a signal produced by reflecting the excitation beam off of a mirror surface at the sample. Since optical delay is negligible (<1ns), any measured delay can be attributed to latent delays in the system electronics (detectors and amplifiers).This calibration is performed before PLIM imaging and included in the lifetime calculations.

C.4 Preparation and demonstration of phosphorescence quenching $Ru(dpp3)^{2+}$ encapsulated nanomiscelles:

Water soluble $Ru(dpp_3)^{2+}$-pluronics nanomicelles were prepared [80]. For the solution, 4 mg of $Ru(dpp_3)Cl_2$ (Alfa Aesar) was dissolved in 100 μl of chloroform and added to 5 ml of Pluronic F68 or F127 (2 wt. %) aqueous solution. The solution was pre-emulsified by stirring for 15 min, followed by 15 min agitation in an ultrasonic bath (150 W). After producing the microemulsion,

the chloroform was evaporated off by stirring the mixture while heating in a regulated 50°C bath for 30 minutes.

Phosphorescent quenching of $Ru(dpp3)^{2+}$ encapsulated in pluronic nanomicelles was demonstrated by comparing the measured phosphorescence lifetimes of pools of oxygenated and deoxygenated dye. Two 100 μL well slides were filled with the dye solution. An excess of enzymatic system for oxygen removal (glucose/glucose oxidase/catalase) was added to one of the wells before both were sealed. The measured lifetime for the oxygenated and deoxygenated solution were 1.5μs (oxygen quenching at atmosphere) and 2.0μs (oxygen depletion), respectively. The lifetime values are within a factor of 2 of the lifetime of $Ru(Dpp_3)^{2+}$ dissolved in ethylene glycol [61], however additional work is needed to properly characterize this dye-nanomicelle dissolved in water if it is to be used as an oxygen sensing probe.

C.5 Animal preparation and surgery:

All animal procedures were reviewed and approved by the Cornell Institutional Animal Care and Use Committee. FVB/n (Charles River Laboratories) and (Tg(ACTB-DsRed*MST)1Nagy/J) mice were anesthetized using isoflurane (MWI) (4% in O2 for induction, 1.5 – 2 % in O2 for surgery and imaging) and was hydrated with 50 μL/ hour subcutaneous injections of 5% glucose (Sigma) in saline (MWI). Body temperature was maintained with a feedback-controlled heat blanket (Harvard Apparatus). Prior to surgery, glycopryllate and dexamethasome were administered by intramuscular injections to quadriceps. After the skull was exposed and cleaned with ethanol (70%) and ferric chloride (10%, VWR), a custom built metal plate was attached to the skull using a cyanocrylate-based glue (Loctite-495) and dental cement

(A-M Systems). A 4-mm diameter craniotomy was centered 2 mm posterior and lateral to the Bregma point. The dura was left intact. A 5-mm diameter glass coverslip (Electron Microscopy Sciences) was used to seal the craniotomy.

REFERENCES

[1] W. R. Zipfel, R. M. Williams and W. W. Webb, "Nonlinear magic: multiphoton microscopy in the biosciences," *National Biotechnology*, vol. 21, pp. 1369-77, 2003.

[2] J. Pawley, Handbook of Biological Confocal Microscopy, New York: Plenum Press, 1990.

[3] H. K. M. C. P. Richard F. Spaide, "Enhanced Depth Imaging Spectral-Domain Optical Coherence Tomography," *American Journal of Ophthalmology,* vol. 146, no. 4, pp. 496-500, 2008.

[4] D. Kobat, M. E. Durst, N. Nishimura, A. W. Wong, C. B. Schaffer, C. Xu and N. Nishumura, "Deep Tissue Multiphoton Microscopy Using Longer Wavelength Excitation," *Optics Express,* vol. 17, no. 16, pp. 13354-13364, 2009.

[5] Y. Wu, P. Xi, J. Y. Qu, T.-H. Cheung and M.-Y. Yu, "Depth-resolved fluorescence spectroscopy of normal and dysplastic cervical tissue," *Optics Express,* vol. 13, no. 2, pp. 382-388, 2005.

[6] M. C. Skala, J. M. Squirrell, K. M. Vrotsos, J. C. Eickhoff, A. Gendron-Fitzpatrick, K. W. Eliceiri and N. Ramanujam, "Multiphoton microscopy of endogenous fluorescence differentiates normal, precancerous, and cancerous squamous epithelial tissues," *Cancer Research,* vol. 65, no. 4, pp. 1180-1186, 2005.

[7] W. R. Zipfel, R. M. Williams, R. Christie, A. Y. Nikitin, B. T. Hyman and W. W. Webb, "Live tissue intrinsic emission microscopy using multiphoton-excited native fluorescence and second harmonic generation.," *Proceedings of the National Academy of Sciences of the United States of America,* vol. 100, no. 12, pp. 7075-7080, 2003.

[8] S. W. Hell and J. Wichmann, "Breaking the diffraction resolution limit by stimulated emission: stimulated-emission-depletion fluorescence microscopy," *Optics Letters,* vol. 19, no. 11, pp. 780-782, 1994.

[9] S. T. Hess, T. P. K. Girirajan and M. D. Mason, "Ultra-High Resolution Imaging by Fluorescence Photoactivation Localization Microscopy," *Biophysical Journal,* vol. 91, no. 11, pp. 4258-4272, 2006.

[10] R. F. Begley, A. B. Harvey and R. L. Byer, "Coherent Anti-Stokes Ramen Spectroscopy," *Applied Physics Letters,* vol. 25, no. 387, 1974.

[11] C. W. Freudinger, W. Min, B. G. Saar, S. Lu, G. R. Holtom, C. He, J. C. Tsai, J. X. Kang and S. X. Xie, "Label-Free Biomedical Imaging with High Sensitivity by Stimulated Raman Scattering Microscopy," *Science,* vol. 322, no. 5909, pp. 1857-1861, 2008.

[12] M. E. Durst, G. Zhu and C. Xu, "Simultaneous spatial and temporal focusing in nonlinear microscopy," *Optics Communications,* vol. 281, no. 7, p. 1796–1805, 2008.

[13] G. Zhu, J. van Howe, M. Durst, W. Zipfel and W. Xu, "Simultaneous spatial and temporal focusing of femtosecond pulses," *Optics Express,* vol. 13, no. 6, pp. 2153-2159, 2005.

[14] D. Oron, E. Tal and Y. Silberberg, "Scanningless depth-resolved microscopy," *Optics Express,* vol. 13, no. 5, pp. 1468-1476, 2005.

[15] A. Leray and J. Mertz, "Rejection of two-photon fluorescence background in thick tissue by differential aberration imaging," *Optics Express,* vol. 14, pp. 10565-10573, 2006.

[16] D. Oron and Y. Silberberg, "Spatiotemporal coherent control using shaped, temporally focused pulses," *Optics Express,* vol. 13, no. 24, pp. 9903-9908, 2005.

[17] M. O. Cambaliza and C. Saloma, "Advantages of two-color excitation fluorescence microscopy with two confocal excitation beams," *Optics Communications,* vol. 184, no. 1-4, p. 25–35, 2000.

[18] D. Kobat, G. Zhu and C. Xu, "Background Reduction with Two-Color Two-Beam Multiphoton Excitation," in *Biomedical Optics*, St. Petersburg, Florida, 2008.

[19] S. Lindek and E. H. K. Stelzer, "Resolution improvement by nonconfocal theta microscopy," *Optics Letters,* vol. 24, no. 21, pp. 1505-1507, 1999.

[20] L. Moreaux, O. Sandre and J. Mertz, "Membrane imaging by second-harmonic generation microscopy," *Journal of* .

[21] J. Mertz and L. Moreaux, "Second-harmonic generation by focused excitation of inhomogeneously distributed scatterers," *Optics Communications,* vol. 196, no. 1-6, p. 325–330, 2001.

[22] R. M. Williams, W. R. Zipfel and W. W. Webb, "Interpreting Second-Harmonic Generation Images of Collagen I Fibrils," *Biophysics Journal,* vol. 88, no. 2, p. 1377–1386, 2005.

[23] D. Oron and Y. Silberberg, "Harmonic generation with temporally focused ultrashort pulses," *Journal of the Optical Society of America B,* vol. 22, no. 12, pp. 2660-2663, 2005.

[24] S.-W. Chu, S.-P. Tai, T.-M. Liu, C.-K. Sun and C.-H. Lin, "Selective imaging in second-harmonic-generation microscopy with anisotropic radiation," *Journal of Biomedical Optics Letters,* vol. 14, no. 1, pp. 010504-(1-3), 2009.

[25] A. Vaziri, J. Tang, H. Shroff and C. Shank, "Multilayer three-dimensional super resolution imaging of thick biological samples," *Proceedings of the National Academy of Sciences of the United States of America,* vol. 105, no. 51, p. 20221–20226, 2008.

[26] B. A. Flusberg, J. C. Jung, E. D. Cocker, E. P. Anderson and M. J. Schnitzer, "In vivo brain imaging using a portable 3.9 gram two-photon fluorescence microendoscope," *Optics Letters,* vol. 30, no. 17, pp. 2272-2274, 2005.

[27] L. Fu, A. Jain, H. Xie, C. Cranfield and M. Gu, "Nonlinear optical endoscopy based on a double-clad photonic crystal fiber and a MEMS mirror," *Optics Express,* vol. 14, no. 3, pp. 1027-1032, 2006.

[28] F. Helmchen, M. S. Fee, D. W. Tank and W. Denk, "A miniature head-mounted two-photon microscope. high-resolution brain imaging in freely moving animals.," *Neuron,* vol. 31, no. 6, pp. 903-912, 2001.

[29] E. J. Botcherby, R. Juskaitis, M. J. Booth and T. Wilson, "Aberration-free optical refocusing in high numerical aperture microscopy," *Optics Letters,* vol. 32, no. 14, pp. 2007-2009, 2007.

[30] V. Nikolenko, B. O. Watson, R. Araya, A. Woodruff, D. S. Peterka and R. Yuste, "SLM Microscopy: Scanless Two-Photon Imaging and Photostimulation with Spatial Light Modulators.," *Frontiers in Neural Circuits,* vol. 2, no. 5, 2008.

[31] G. J. Tearney, M. E. Brezinski, B. E. Bouma, S. A. Boppart, C. Pitris, J. F. Southern and J. G. Fujimoto, "In vivo endoscopic optical biopsy with optical coherence tomography," *Science,* vol. 276, no. 5321, pp. 2037-2039, 1997.

[32] R. Du, K. Bi, S. Zeng, D. Li, S. Xue and Q. Luo, "Analysis of fast axial scanning scheme using temporal focusing with acousto-optic deflectors," *Journal of Modern Optics,* vol. 56, pp. 99-102, 2008.

[33] R. L. Fork, O. E. Martinez and J. P. Gordon, "Negative dispersion using pairs of prisms," *Optics Letters,* vol. 9, no. 5, pp. 150-152, 1984.

[34] O. E. Martinez, "3000 times grating compressor with positive group velocity dispersion: Application to fiber compensation in 1.3-1.6 μm region," *IEEE Journal of Quantum Electronics,* vol. 23, no. 1, pp. 59-64, 1987.

[35] P. Tournois, "Acousto-optic programmable dispersive filter for adaptive compensation of group delay time dispersion in laser systems," *Optics Communications,* vol. 140, no. 4-6, pp. 245-249, 1997.

[36] A. M. Weiner, D. E. Leaird, J. S. Patel and J. R. Wullert, "Programmable femtosecond pulse shaping by use of a multielement liquid-crystal phase modulator," *Optics Letters,* vol. 15, no. 6, pp. 326-328, 1990.

[37] E. Zeek, K. Maginnis, S. Backus, U. Russek, M. Murnane, G. Mourou, H. Kapteyn and G. Vdovin, "Pulse compression by use of deformable mirrors," *Optics Letters,* vol. 24, no. 7, pp. 493-495, 1999.

[38] C. Radzewicz, P. Wasylczyk, W. Wasilewski and J. S. Krasiski, "Piezo-driven deformable mirror for femtosecond pulse shaping," *Optics Letters,* vol. 29, no. 2, pp. 177-179, 2004.

[39] Q. Li, M. Lovell, J. Mei and W. Clark, "A Study of Displacement Distribution in a Piezoelectric Heterogeneous Bimorph," *Journal of Mechanical Design,* vol. 126, no. 4, 2004.

[40] M. R. Steel, F. Harrison and P. G. Harper, "The piezoelectric bimorph: An experimental and theoretical study of its quasistatic response," *Journal of Physics D: Applied Physics,* vol. 11, no. 979, pp. 979-989, 1978.

[41] P. Wnuk, C. Radzewicz and J. S. Krasinski, "Bimorph piezo deformable mirror for femtosecond pulse shaping," *Optics Express,* vol. 13, no. 11, pp. 4154-4159, 2005.

[42] Piezo Systems, Inc., "Introduction to piezo transducers," 2007. [Online]. Available: http://www.piezo.com/tech2intropiezotrans.html. [Accessed 24 June 2009].

[43] J. A. Palero, H. S. de Bruijin, A. van der Ploeg van den Heuvel, H. J. Sterenborg and H. C. Gerritsen, "Spectrally resolved multiphoton imaging of in vivo and excised mouse skin tissues," *Biophysics Journal,* vol. 93, no. 3, pp. 992-1007, 2007.

[44] S. P. Gross, "Application of optical traps in vivo," *Methods in Enzymology,* vol. 361, pp. 162-174, 2003.

[45] K. C. Neuman and S. M. Block, "Optical trapping," *The Review of Scientific Instruments,* vol. 75, no. 9, pp. 2787-2809, 2004.

[46] A. Draaijer, R. Sanders and H. C. Gerristen, "Fluorescence Lifetime Imaging, a New Tool in Confocal Microscopy," in *Handbook of Biological Confocal Microscopy*, J. B. Pawley, Ed., New York, Plenum Press, 1995, pp. 491-505.

[47] H. Wallrabe and A. Periasamy, "Imaging protein molecules using FRET and FLIM microscopy," *Curr. Opin. Biotechnol.*, vol. 16, no. 1, p. 19–27, 2004.

[48] W. Zhong, P. Urayama and M. A. Mycek, "Imaging fluorescence lifetime modulation of a ruthenium-based dye in living cells: the potential for oxygen sensing," *J Phys D: Appl Phys*, vol. 36, pp. 1689-1695, 2003.

[49] E. Gratton, S. Breusegem, J. Sutin, Q. Ruan and N. Barry, "Fluorescence lifetime imaging for the two-photon microscope: time-domain and frequency-domain methods," *J. Biomed. Opt*, vol. 8, p. 381, 2003.

[50] S. Sakadžić, E. Roussakis, M. A. Yaseen, E. T. Mandeville, V. J. Srinivasan, K. Arai, S. Ruvinskaya, A. Devor, E. H. Lo, S. A. Vinogradov and D. A. Boas, "Two-photon high-resolution measurement of partial pressure of oxygen in cerebral vasculature and tissue," *Nat. Methods*, vol. 7, no. 9, p. 755–759, 2010.

[51] J. Lecoq, A. P, E. R, M. D, Y. G. H, S. A. V and S. C, "Simultaneous two-photon imaging of oxygen and blood flow in deep cerebral vessels," *Nat. Medicine*, vol. 17, no. 7, pp. 893-898, 2011.

[52] G. J. Brakenhoff, J. Squier, T. Norris, A. Bliton, M. Wade and B. Athey, "Real-time two-photon confocal microscopy using a femtosecond, amplified Ti:sapphire system," *J. Microsc.*, vol. 181, p. 253–259, 1996.

[53] A. Buist, M. Muller, J. Squier and G. Brakenhoff, "Real-time two-photon absorption microscopy using multipoint excitation," *J. Microsc.*, vol. 192, no. 2, pp. 217-226, 1998.

[54] M. Fricke and T. Nielsen, "Two-dimensional imaging without scanning by multifocal multiphoton microscopy," *Appl Opt*, vol. 44, no. 15, pp. 2984-2988, 2005.

[55] D. D.-U. Li, S. Ameer-Beg, J. Arlt, D. Tyndall, R. Walker, D. R. Matthews, V. Visitkul, J. Richardson and R. K. Henderson, "Time-Domain Fluorescence Lifetime Imaging Techniques Suitable for Solid-State Imaging Sensor Arrays," *Sensors*, vol. 12, pp. 5650-5669, 2012.

[56] D. Li, J. Arlt, J. Richardson, R. Walker, A. Buts, D. Stoppa, E. Charbon and R. Henderson, "Real-time fluorescence lifetime imaging system with a 32 × 32 0.13 μm CMOS low dark-count single-photon avalanche diode array," *Opt. Express,* vol. 18, p. 10257–10269, 2010.

[57] D. Li, J. Arlt, D. Tyndall, R. Walker, J. Richardson, D. Stoppa, E. Charbon and R. K. Henderson, "Video-rate fluorescence lifetime imaging camera with CMOS single-photon avalanche diode arrays and high-speed imaging algorithm," *J. Biomed. Opt.*, vol. 16, p. 096012, 2011.

[58] P. Hartmann and W. Ziegler, "Lifetime Imaging of Luminescent Oxygen Sensors Based on All-Solid-State Technology," *Anal. Chem.*, vol. 68, pp. 4512-4514, 1996.

[59] S. Sakadžić, S. Yuan, E. Dilekoz, S. Ruvinskaya, S. A. Vinogradov, C. Ayata and D. A. Boas, "Simultaneous imaging of cerebral partial pressure of oxygen and blood flow during functional activation and cortical spreading depression," *Appl Opt*, vol. 48, no. 10, pp. D169-D177, 2009.

[60] I. Dunphy, S. A. Vinogradov and D. F. Wilson, "Oxyphor R2 and G2: phosphors for measuring oxygen by oxygen-dependent quenching of phosphorescence," *Anal Biochem,* vol. 310, no. 2, pp. 191-198, 2002.

[61] K. J. Morris, M. S. Roach, W. Xu, J. N. Demas and B. A. DeGraff, "Luminescence Lifetmie Stadnards for the Nanosecond to Microsecond Range and Oxygen Quenching of Ruthenium (II) Complexes," *Anal Chem,* vol. 89, pp. 9310-9314, 2007.

[62] O. S. Finikova, A. Y. Lebedev, A. Aprelev, T. Troxler, F. Gao, C. Garnacho, S. Muro, R. M. Hochstrasser and S. A. Vinogradova, "Oxygen Microscopy by Two-Photon-Excited Phosphorescence," *ChemPhysChem,* vol. 9, no. 12, pp. 1673-1679, 2008.

[63] H. Szmacinski, I. Gryczynski and J. R. Lakowicz, "Spatially Localized Ballistic Two-Photon Excitation in Scattering Media," *Biospectroscopy*, vol. 4, p. 303–310, 1998.

[64] P. Theer and W. Denk, "On the fundamental imaging-depth limit in two-photon microscopy," *JOSA A,* vol. 23, no. 12, pp. 3139-3149, 2006.

[65] J. S. Sanders, R. G. Driggers, C. E. Halford and S. T. Griffin, "Imaging with frequency-modulated reticles," *Opt. Eng.,* vol. 30, no. 11, pp. 1720-1724, 1991.

[66] S. S. Howard, A. A. Straub and C. Xu, "Multiphoton modulation microscopy for high-speed deep biological imaging," *IEEE/OSA Conf. Lasers Electro-Optics (CLEO),* p. CWD6, 2010.

[67] G. Futia, P. Schlup, D. G. Winters and R. A. Bartels, "Spatially-chirped modulation imaging of absorption and fluorescent objects on single-element optical detector," *Opt. Express,* vol. 19, no. 2, pp. 1626-1640, 2011.

[68] J. Philip and K. Carlsson, "Theoretical investigation of the signal-to-noise ratio in fluorescence lifetime imaging," *J Opt Soc Am A,* vol. 20, no. 2, pp. 368-379, 2003.

[69] G. I. Redford and R. M. Clegg, "Polar Plot Representation for Frequency-Domain Analysis of Fluorescence Lifetimes," *J Fluoresc,* vol. 15, no. 5, 2005.

[70] S. M. R. M. Nezam, "High-speed polygon-scanner-based wavelength-swept laser source in the telescope-less configurations with application in optical coherence tomography.," *Optics Letters,* vol. 33, pp. 1741-1743, 2008.

[71] M. Chen, Z. Ding, L. Wang, T. Wu and B. Wang, "Wavelength-swept laser around 1300 nm based on polygon filter in Littrow telescope-less configuration.," in *SPIE*, 2010.

[72] M. Intaglietta, P. C. Johnson and R. M. Winslow, "Microvascular and tissue oxygen distribution," *Cardiovalscular Research,* vol. 32, pp. 632-643, 1996.

[73] Physik Instrumente, [Online]. Available: http://www.physikinstrumente.com. [Accessed 4 August 2014].

[74] R. Salome, Y. Kremer, S. Dieudonne, J. F. Leger, O. Krichevsky, C. Wyart, D. Chatenay and L. Bourdieu, "Ultrafast random-access scanning in two-photon microscopy using acousto-optic deflectors," *Journal of Neuroscience Methods,* vol. 154, no. 1-2, pp. 161-174, 2006.

[75] D. R. Gaddum and P. Saggau, "Fast three-dimensional laser scanning scheme using acousto-optic deflectors," *Journal of Biomedical Optics,* vol. 10, no. 6, 2005.

[76] G. Katona, G. Szalay, P. Maak, A. Kaszas, M. Veress, D. Hillier, B. Chiovini, E. S. Vizi, B. Roska and B. Rozsa, "Fast two-photon in vivo imaging with three-dimensional random-access scanning in large tissue volumes," *Nature Methods,* vol. 9, no. 2, pp. 201-211, 2012.

[77] A. Mermillod-Blondin, E. McLeod and C. B. Arnold, "High-speed varifocal imaging with a tunable acoustic gradient index of refraction lens," *Optics Letters,* vol. 33, pp. 2146-2148, 2008.

[78] H. Dana, A. Marom, S. Paluch, R. Dvorkin, I. Brosh and S. Shoham, "Hybrid multiphoton volumetric functional imaging of large-scale bioengineered neuronal networks," *Nature Communications,* vol. 5, 2014.

[79] L.-C. Cheng, C.-Y. Chang, C.-Y. Lin, K.-C. Cho, W.-C. Yen, N.-S. Chang, C. Xu, C. Y. Dong and S.-J. Chen, "Spatiotemporal focusing-based widefield multiphoton microscopy for fast optical sectioning," *Optics Express,* vol. 20, no. 8, pp. 8939-8948, 2012.

[80] M. Maurin, O. Stephan, J. C. Vial, S. R. Marder and B. van der Sanden, "Deep in vivo two-photon imaging of blood vessels with a new dye encapsulated in pluronic nanomicelles," *J Biomed Opt,* vol. 16, no. 3, p. 036001, 2011.

[81] W. Denk, J. H. Strickler and W. W. Webb, "Two-photon laser scanning fluorescence microscopy," *Science,* vol. 248, pp. 73-76, 1990.

[82] D. Kobat, N. G. Horton and C. Xu, "In vivo two-photon microscopy to 1.6-mm depth in mouse cortex," *J. Biomed. Opt.,* vol. 16, p. 106014, 2011.

[83] R. Kiesslich, J. Burg, M. Vieth, J. Gnaendiger, M. Enders, P. Delaney, A. Polglase, W. McLaren, D. Janell, S. Thomas, B. Nafe, P. R. Galle and M. F. Neurath, "Confocal laser endoscopy for diagnosing intraepithelial neoplasias and colorectal cancer in vivo.," *Gastroenterology,* vol. 127, no. 3, pp. 706-713, 2004.

[84] J. Phillip and K. Carlsson, "Theoretical investigation of the signal-to-noise ratio in fluorescence lifetime imaging," *Journal of the Optical Society of America,* vol. 20, no. 2, 2003.